Article

Current Biology

The Foveal Visual Representation of the Primate Superior Colliculus

Highlights

- Primate superior colliculus (SC) is highly sensitive to foveal visual input
- SC visually sensitive neurons sample foveolar visual space non-uniformly
- SC magnifies foveal visual images in neural tissue as much as primary visual cortex
- Tiny foveal stimuli activate large SC tissue area due to fixational eye movements

Authors

Chih-Yang Chen, Klaus-Peter Hoffmann, Claudia Distler, Ziad M. Hafed

Correspondence

ziad.m.hafed@cin.uni-tuebingen.de

In Brief

Chen et al. show that superior colliculus (SC) is highly sensitive to foveal visual input and that it magnifies foveal image representation much more than previously anticipated. Their topography data, with large foveal magnification, show that tiny foveal stimuli can activate a large portion of SC neural tissue due to fixational eye movements.

Chen et al., 2019, Current Biology *29*, 2109–2119
July 8, 2019
https://doi.org/10.1016/j.cub.2019.05.040

CellPress

Current Biology
Article

The Foveal Visual Representation of the Primate Superior Colliculus

Chih-Yang Chen,[1,2] Klaus-Peter Hoffmann,[3] Claudia Distler,[4] and Ziad M. Hafed[1,2,5,*]
[1]Werner Reichardt Centre for Integrative Neuroscience, Tuebingen University, Tuebingen 72076, Germany
[2]Hertie Institute for Clinical Brain Research, Tuebingen University, Tuebingen 72076, Germany
[3]Research Department of Neuroscience, Ruhr University Bochum, Bochum 44801, Germany
[4]Department of General Zoology and Neurobiology, Ruhr University Bochum, Bochum 44801, Germany
[5]Lead Contact
*Correspondence: ziad.m.hafed@cin.uni-tuebingen.de
https://doi.org/10.1016/j.cub.2019.05.040

SUMMARY

A defining feature of the primate visual system is its foveated nature. Processing of foveal retinal input is important not only for high-quality visual scene analysis but also for ensuring precise, albeit tiny, gaze shifts during high-acuity visual tasks. The representations of foveal retinal input in the primate lateral geniculate nucleus and early visual cortices have been characterized. However, how such representations translate into precise eye movements remains unclear. Here, we document functional and structural properties of the foveal visual representation of the midbrain superior colliculus. We show that the superior colliculus, classically associated with extra-foveal spatial representations needed for gaze shifts, is highly sensitive to visual input impinging on the fovea. The superior colliculus also represents such input in an orderly and very specific manner, and it magnifies the representation of foveal images in neural tissue as much as the primary visual cortex does. The primate superior colliculus contains a high-fidelity visual representation, with large foveal magnification, perfectly suited for active visuomotor control and perception.

INTRODUCTION

A tiny portion (~1% or 2%) of our retina, the fovea, contains the highest photoreceptor density [1] while, at the same time, commanding large neural tissue magnification as signals traverse from retina to lateral geniculate nucleus and primary visual cortex (V1) [2]. Such magnification confers on foveal input a tremendous computational advantage compared to images sampled extra-foveally. As a result, we frequently move our eyes to align tiny portions of our visual environment with our fovea; the fovea represents the "origin" of our visual space, and most of our visually guided eye-movement behavior (e.g. during reading, sewing, driving) involves aligning this "origin" with what currently matters most.

Despite the importance of foveal visual processing, and despite the suitability of primates for investigating it [3–12], studies of foveal visual mechanisms have become increasingly rare in the past 3 or 4 decades. This is primarily due to challenges associated with studying foveal vision: foveal retinal ganglion cells often have response fields (RFs) that are the size of single photoreceptors [6, 13]; thus, even tiny fixational eye movements can displace images away from RFs, and this can affect downstream areas that spatially pool retinal ganglion cell information. Paradoxically, a historical shift toward studying extra-foveal eccentricities in perception and cognition was simultaneously accompanied [14] by an assumption that fixational eye movements in between gaze shifts are irrelevant. Because we now know that this is an oversimplification [14, 15], there is an ever-pressing need to investigate foveal processing mechanisms.

Such a need is especially relevant for sensory-motor areas, like superior colliculus (SC), that are at the nexus of both visual processing and eye movement generation. The SC is instrumental for generating microsaccades [16, 17], which precisely re-direct gaze during foveal vision [18–20] and which also influence peripheral eccentricities [15, 21]. However, it is not known how microscopic gaze control can be guided visually; the SC's foveal visual representation is virtually unexplored. Our purpose here was to characterize the physiological and structural properties of SC foveal vision; we show that SC is as foveal a visual structure as V1.

RESULTS

Primate SC Is Highly Sensitive to Foveal Visual Input

We recorded from 413 neurons, well-isolated (Figure S1A) and characterized online, in awake macaque monkeys N and P. We characterized RF hotspot location (the point for which maximal visual response was evoked), RF area, and other visual response properties by presenting light spots over a uniform background. We carefully controlled for image shifts caused by fixational eye movements (STAR Methods).

We first identified SC sites containing neurons sensitive to foveal stimuli. Figures S1B and S1C show that RF hotspots <1 or 2 degrees in eccentricity tiled the entire foveal region contralateral to the recorded SC. This was also true for anesthetized monkeys R and F, recorded in separate experiments (Figures S1D and S1E; STAR Methods). Therefore, primate SC has clear access to foveal visual input.

We examined foveal visual RFs in the awake animals by plotting peak stimulus-evoked response as a function of stimulus location (Figure 1A, top row showing 4 example neurons

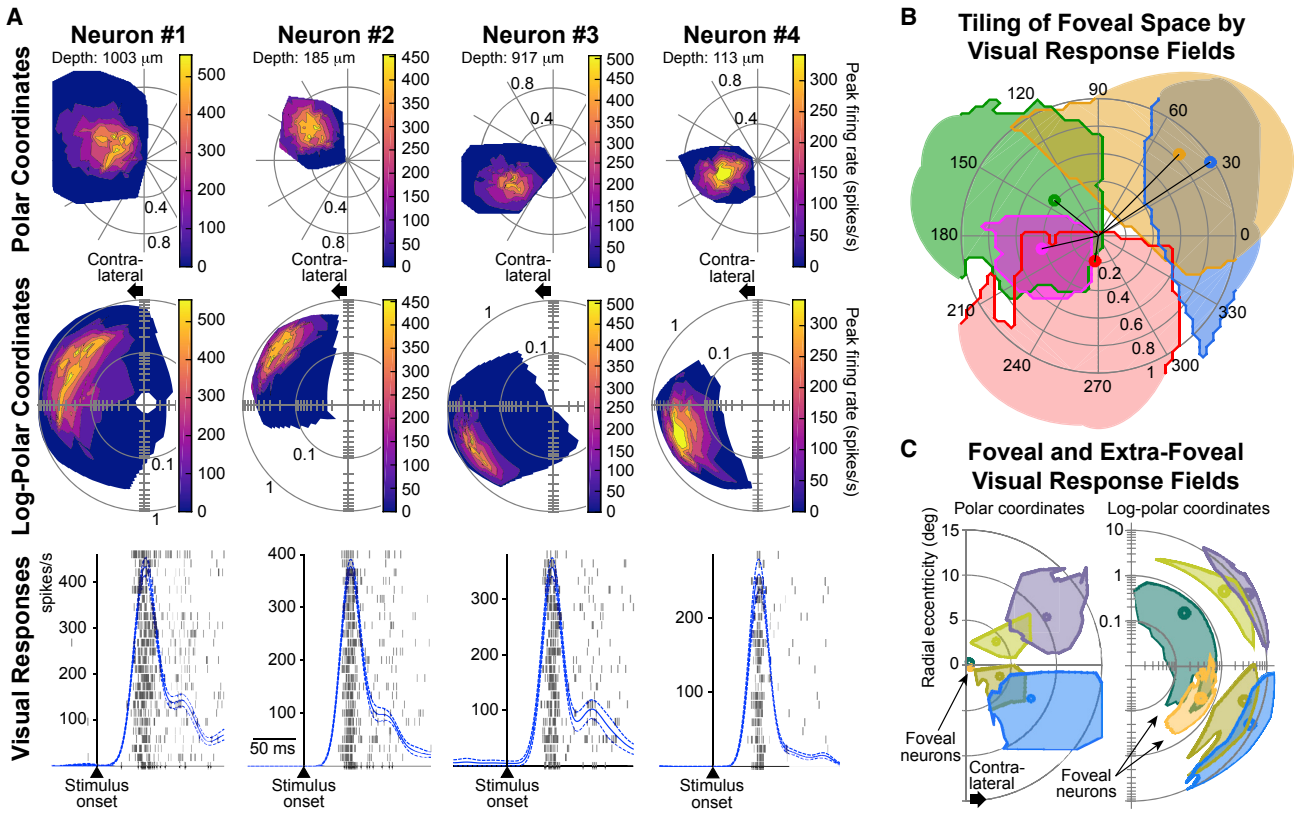

Figure 1. Foveal Visual Neurons of Primate SC

(A) Four neurons from right SC in awake monkeys. (Top row) Visual response fields (RFs) in polar coordinates are shown. (Middle row) Same RFs using log-polar coordinates magnifying small eccentricities are shown [16]. (Bottom row) Raw firing rates (blue) along with SEM error bars (dashed blue) when a stimulus was presented near the neuron's RF hotspot are shown. Individual rasters show raw spike (action potential) times across stimulus repetitions. All neurons had highly sensitive RFs almost entirely contained within the foveola (i.e., <0.5-degree eccentricity) [6–8, 22].

(B) Across both right and left SCs, the entire foveal space was represented. Each small circle indicates RF hotspot location from a neuron; solid lines indicate RF inner boundaries.

(C) Foveal RFs were much smaller than peripheral ones. Six example neurons are shown with RF boundaries and hotspot locations indicated by outlines and small circles, respectively.

Also see Figures 2A, S1, S2, and S4.

mapped with the Fixation visual RF mapping task; STAR Methods). We observed small, highly sensitive visual RFs. All 4 neurons in Figure 1A had RFs almost entirely contained within the rod-sparse foveola region of the retinal image (i.e., eccentricities <0.5 degree), suggesting access to the highest acuity portion of visual input. The middle row of Figure 1A plots the same visual RFs using log-polar coordinates [16] to magnify small eccentricities; it demonstrates that, despite the proximity of all neural RFs to gaze line of sight, the inner borders of all RFs were well defined. Thus, SC foveal visual RFs sample highly specific regions of the visual image.

Foveal SC neurons were also particularly light sensitive (Figure 1A, bottom row; each spike raster shows responses from an individual trial, and the stacked trials show responses from the 25 nearest locations to each neuron's RF hotspot). The particular neurons shown in Figure 1A had zero baseline activity (typical of SC neurons; Figure S2A) and only responded when light impinged on a small foveal region. Their high sensitivity was consistent across the population and similar to sensitivity in more eccentric neurons (Figure S2B). Some neurons (e.g., neurons no. 1, no. 2, and no. 3) showed a small, secondary subsequent burst, which had an RF similar to that of the primary burst. Thus, SC not only has access to foveolar (i.e., rod-sparse) image regions, but it is also highly sensitive to them.

Strong visual sensitivity was additionally reflected in neural response latency [23–26]: first-spike latency (STAR Methods) was similar to that in peripheral neurons (Figure S2C). Only in superficial SC layers, response latency decreased with increasing foveal eccentricity (Figure S2C, blue). Because superficial neurons receive direct retinal input [3–5], this non-uniformity could reflect the sparseness of rod photoreceptors (which have fast integration times) in foveola [6, 27].

Foveal SC Samples Visual Space Non-uniformly, even within Foveola

The fact that foveal SC neurons have well-defined RFs (Figure 1A) suggests that the population as a whole can achieve full coverage of foveal image regions. We observed this not only in hotspot locations (Figures S1B–S1E) but also when we examined individual RF areas (Figure 1B). The neurons exhibited

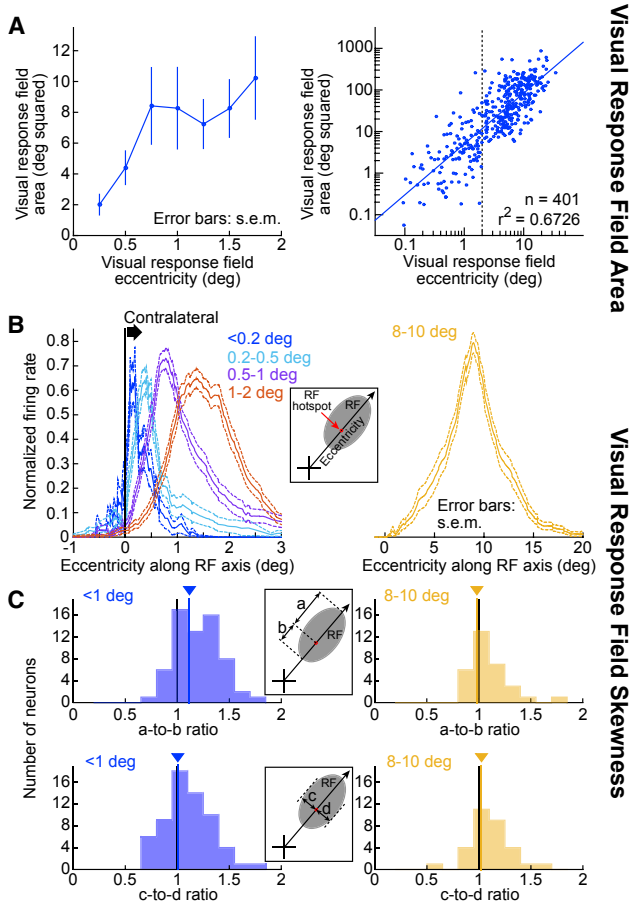

Figure 2. Non-uniform SC Foveal Sampling

(A) (Left) Visual RF area depended on eccentricity (awake monkeys N and P; p = 0.044; one-way ANOVA; F = 2.782; n = 121 neurons). (Right) RF areas from both foveal and eccentric neurons (dots) together are shown. Foveal neurons (e.g., <2 degrees, dashed line) formed a continuum with peripheral ones.

(B) Non-uniform spatial sampling even within individual RFs. We binned neurons according to their preferred eccentricity (color coded). For each bin, we plotted one-dimensional normalized RF profiles along the radial axis (inset). Foveal neurons (left panel) became increasingly skewed with decreasing eccentricity; there was no activity beyond the 0-degree singularity toward the ipsilateral visual field. Each curve shows average normalized firing rate from all neurons within a given bin, along with SEM across neurons.

(C) (Top row) RF skewness quantified as the ratio of *a*-to-*b* (inset). Foveal neurons (left) had skewed RFs ($p = 3.797 \times 10^{-5}$; Wilcoxon signed rank test against a median of 1); eccentric neurons (right) did not (p = 0.906; Wilcoxon signed rank test against a median of 1). (Bottom row) *c*-to-*d* ratios for the same neurons (inset) are shown. Both foveal (p = 0.504) and eccentric (p = 0.367) neurons did not show significant RF skewness. Solid colored lines indicate median values across the population.

Also see Figures S1, S2, S3, and S4.

classic hallmarks of population coding: tiling of space by RF hotspots as well as RF overlap, like saccade-related activity for larger eccentricities [28].

We were interested in the dependence of such foveal population coding on eccentricity. RF area increases with eccentricity (Figure 1C) [9, 25], like in visual cortices [29]. However, it is assumed that spatial resolution in visual cortices is uniform within the foveal image representation [29]. This is not what we found in SC. There was clear dependence of RF area on foveal eccentricity (Figure 2A, left, awake animals). Moreover, this dependence followed a consistent relationship with extra-foveal neurons (Figure 2A, right). Therefore, there exists a continuum of SC visual representation from well within the rod-sparse foveolar region up to eccentricities two orders of magnitude larger. This non-uniformity of foveal spatial sampling might explain why microsaccades are needed to re-align gaze [18–20, 30]: microsaccade-induced image displacements equivalent to a mere handful of foveal photoreceptors bring images of fine stimuli onto SC RFs with higher spatial resolution (smaller area) than before the movements.

We also confirmed the results of Figure 2A in anesthetized monkeys, from which we recorded the most superficial SC visual laminae (Figures S3A and S3B; STAR Methods). Additionally, we expected microsaccade-related activity [16] to emerge in the awake animals below foveal visual neurons; this was the case (Figure S4). It was also the case that microsaccade-related movement fields sampled foveal space non-uniformly like the visual RFs (Figure S3C), but the movement fields were smaller.

Foveal SC Exhibits Strict Spatial Cutoffs in Representing Contralateral and Ipsilateral Visual Eccentricity

Non-uniformity of SC foveal spatial sampling was not restricted to RF areas. Even individual RFs were strongly skewed. For example, the RF of neuron no. 1 in Figure 1A had a longer activity tail at eccentricities larger than RF hotspot location compared to smaller. We characterized such skewness by plotting RF profiles along a single dimension (eccentricity), connecting the line of sight to a neuron's RF hotspot (Figure 2B, inset). We classified neurons according to their preferred eccentricities (Figure 2B, different colors). As eccentricity decreased, there was increasing RF skewness (Figure 2B, left; compare activity beyond versus nearer than the preferred eccentricity eliciting maximal response in each curve). On the inner edges of RFs, there was a strict cutoff of activity, such that there was no activity on the other side of the "zero" degree discontinuity. This happened even if it meant strong RF skewness (e.g., Figure 2B, left, blue). Even neurons with <0.2 degree preferred eccentricity (Figure 2B, left, blue) were strictly cut off (any residual ipsilateral activity on the other side of zero was due to visual activation by the fixation spot itself, as in Figure 6 below, or unavoidable residual eye-position calibration and/or correction errors).

We quantified RF skewness by measuring distance *a* from RF hotspot location to RF outer border and comparing it to distance *b* from RF hotspot location to RF inner border (Figure 2C, top inset). Foveal SC neurons were significantly skewed (Figure 2C, top left; *a*-to-*b* ratio > 1) when compared to extra-foveal neurons (Figure 2C, top right; *a*-to-*b* ratio = 1). Such skewness was restricted to the eccentricity dimension; measuring RFs along an axis orthogonal to eccentricity (Figure 2C, bottom inset) revealed symmetry (Figure 2C, bottom). Therefore, foveal SC visual responses are strongly lateralized along the eccentricity dimension.

SC Possesses Orderly Topographic Representation of Foveal Visual Space

Computational models [31] suggest that RF skewness (Figure 2) is a hallmark of foveal magnification. We therefore

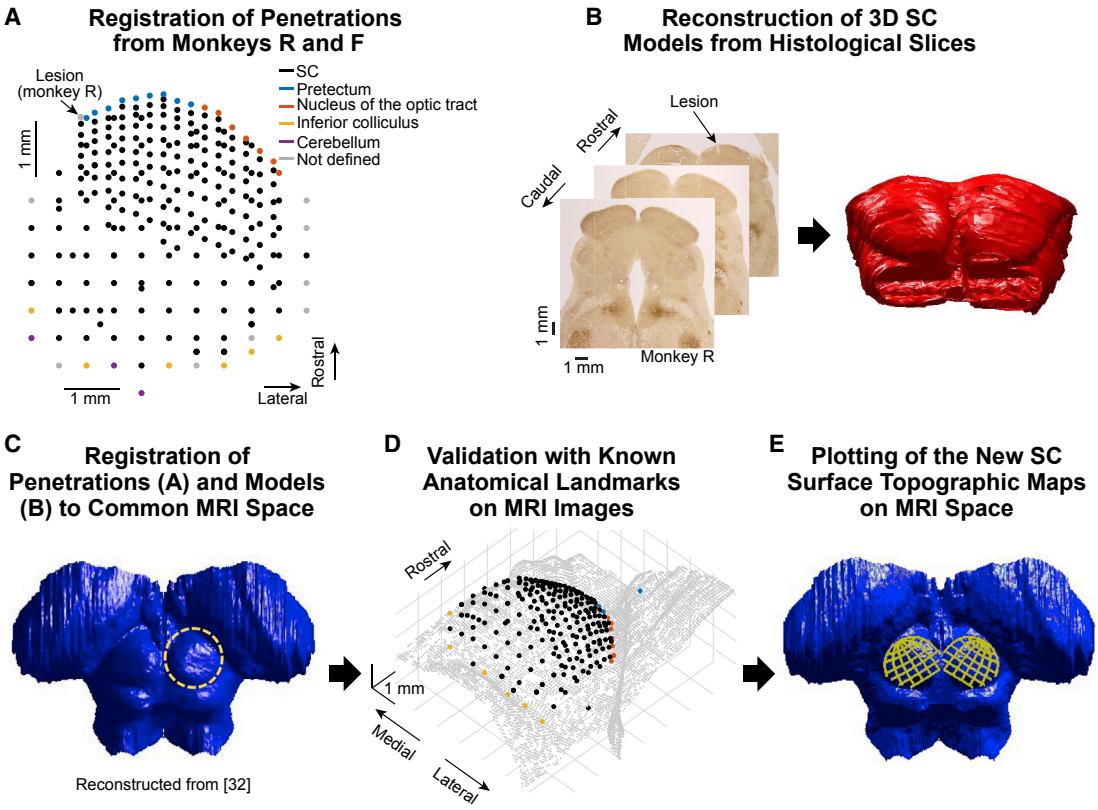

Figure 3. Constructing Three-Dimensional SC Surface Topography

(A) We co-registered dense mappings from monkeys R and F (black dots) and then confirmed that physiologically identified non-SC sites (colors) were at appropriate anatomical locations.

(B) We aligned histological sections using an electrolytic lesion (100 μm rostro-medially to the last visual RF) and then manually traced to generate three-dimensional structure (STAR Methods).

(C) The data were then aligned to a standardized *post mortem* macaque MRI sequence [32].

(D) This allowed us to map our electrode penetrations from (A) to three-dimensional structure and to confirm anatomical landmarks based on SC neighboring structures (see Video S1).

(E) We used our new SC surface topography model (Figures 4 and 5) to describe three-dimensional SC surface topography on a standard macaque MRI (see Video S2). The left SC topography is just a mirror image of the right SC topography generated from our data. Data S1 lists all three-dimensional coordinates for the shown iso-eccentricity and iso-direction lines (right SC).

Also see Videos S1 and S2 and Data S1.

next turned to the question of how SC foveal vision is structurally represented. In anesthetized animals (STAR Methods), we densely sampled the most superficial SC laminae. We then sacrificed the animals and registered our recordings with structural neuroanatomy (Figure 3; Videos S1 and S2; Data S1; STAR Methods). We assessed preferred eccentricities along SC surface (Figure 4A, showing a top-down view; each gray dot is an SC electrode location). We plotted iso-eccentricity lines (color coded) and found orderly SC topography even within the foveal representation. The orderly eccentricity organization was also continuous with extra-foveal eccentricities (Figure 4A; thick red lines show iso-eccentricity lines in our model of SC topography described below). In this analysis, we used a view similar to that used in previous estimates [33] of topography that were based on electrically evoked saccades from the deeper layers [35]. This allowed us to directly compare our data, containing explicit measures of foveal topography, to a classic model [33] only extrapolating from extra-foveal measurements [35]. We also repeated the same analysis for iso-direction lines relative to the horizontal meridian (Figure 4B) and confirmed that we could still find orderly foveal topography even in our awake animals (Figure S5).

Therefore, foveal SC representation not only exists (Figure 1), but it is also organized in highly specific manners, both functionally (Figure 2) and structurally (Figure 4).

SC Magnifies Foveal Visual Representation in Neural Tissue as much as V1

Our dense mappings of Figures 4A and 4B, coupled with strong RF skewness (Figure 2), convinced us that SC contains significantly larger foveal magnification than expected. We therefore fitted our data from Figures 4A and 4B (color-coded lines) with a mathematical function incorporating foveal magnification (Figures 4A and 4B, thick red lines), similar to past descriptions of V1 and SC (STAR Methods). We used

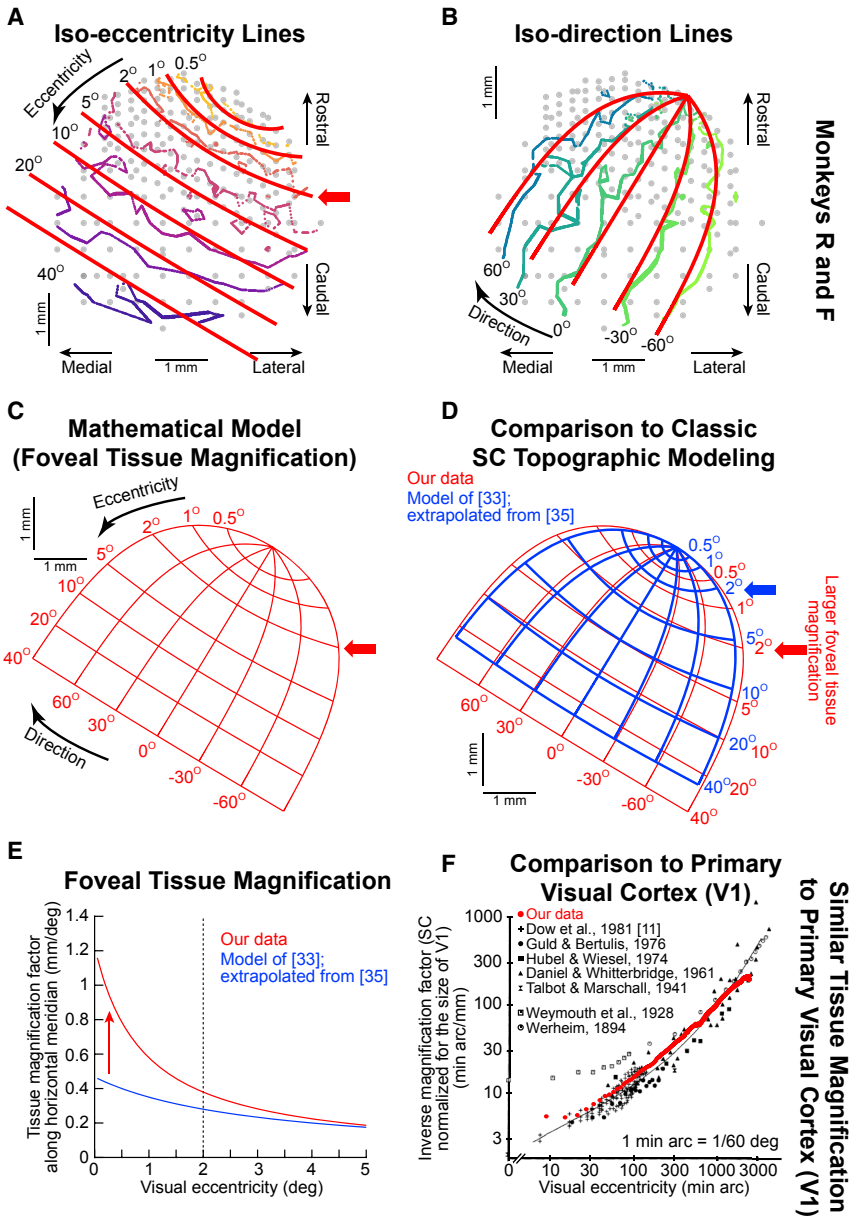

Figure 4. SC Is as Strongly Foveally Magnified as V1

(A) Using dense superficial SC sampling (anesthetized monkeys R and F), we estimated iso-eccentricity lines for right SC. Gray circles denote SC electrode locations (Figure 3). We drew interpolated lines along which neurons preferred a single eccentricity (color-coded according to preferred eccentricity). Foveal eccentricities were anatomically represented in an orderly manner at the rostro-lateral pole. Thick red lines show iso-eccentricity lines in our mathematical model of SC surface topography (C).

(B) Similar analyses for iso-direction lines.

(C) SC surface topography model. The red arrow indicates 2-degree eccentricity; almost 1 mm, or approximately 1/4–1/3, of SC tissue along the horizontal meridian is foveal.

(D) The universally accepted model [33], aligned at the same origin as our model for easier comparison, assumes much smaller foveal magnification (blue map and arrow).

(E) Linear tissue magnification factor [10, 34] along the horizontal meridian. Our data (red) demonstrate larger than two-fold foveal magnification (vertical red arrow).

(F) Our magnification factor curve (plotted in red as "inverse magnification factor," in order to facilitate comparison to the other shown data) [11] was similar to V1 foveal magnification factor (black). Note that we corrected for anatomical size differences between SC and V1 for this comparison (STAR Methods). Our data (red) are superimposed on a meta-analysis adapted, with permission, from [11]. Also see Figures S5, S6, and S7.

the following equations, based on [33], relating tissue space to visual coordinates:

$$X = B_x log_e\left(\frac{\sqrt{R^2 + 2ARcos(\theta) + A^2}}{A}\right) \quad \text{(Equation 1)}$$

$$Y = B_y arctan\left(\frac{Rsin(\theta)}{Rcos(\theta) + A}\right) \quad \text{(Equation 2)}$$

where X and Y are anatomical distances along the SC axis (X being along the axis of the horizontal meridian and Y being along the orthogonal axis); R and θ are visual coordinates in eccentricity (R) and direction from horizontal (θ); and B_x, B_y, and A are model parameters. Our parameter values after fitting were 1.1 (B_x), 1.8 (B_y), and 0.9 (A).

Our data fits (Figure 4C) revealed that the 2-degree eccentricity line was located up to almost 1 mm away from the rostro-lateral "origin" of the topographic map (Figure 4C, red arrow); this indicates that, along the eccentricity dimension, up to 1/4–1/3 of the SC represents foveal eccentricities. This is larger than two-fold the magnification factor extrapolated by classic SC topographic modeling [33]. To demonstrate this, we aligned in Figure 4D both our data (red) and the original extrapolated model [33] (blue). We found a remarkable difference: what the original model predicts as the 5-degree eccentricity line in neural tissue is in reality only the edge of the foveal representation (2 degrees).

We also explicitly calculated magnification factor. In Figure 4E, we estimated linear foveal magnification factor along the horizontal meridian (that is, mm of neural tissue per degree of visual eccentricity) for our data (red) as well as the classic extrapolated model [33] (blue). We confirmed larger than two-fold increase in linear foveal magnification factor in fovea compared to [33]. Note that both models converge at larger eccentricities because larger eccentricities are logarithmically compressed.

We then compared our data for SC foveal magnification to V1. Because V1 is almost an order of magnitude larger than SC, we first scaled our SC measurements to equalize for overall size (STAR Methods). We then plotted our magnification factor measurements along with an extensive meta-analysis of numerous

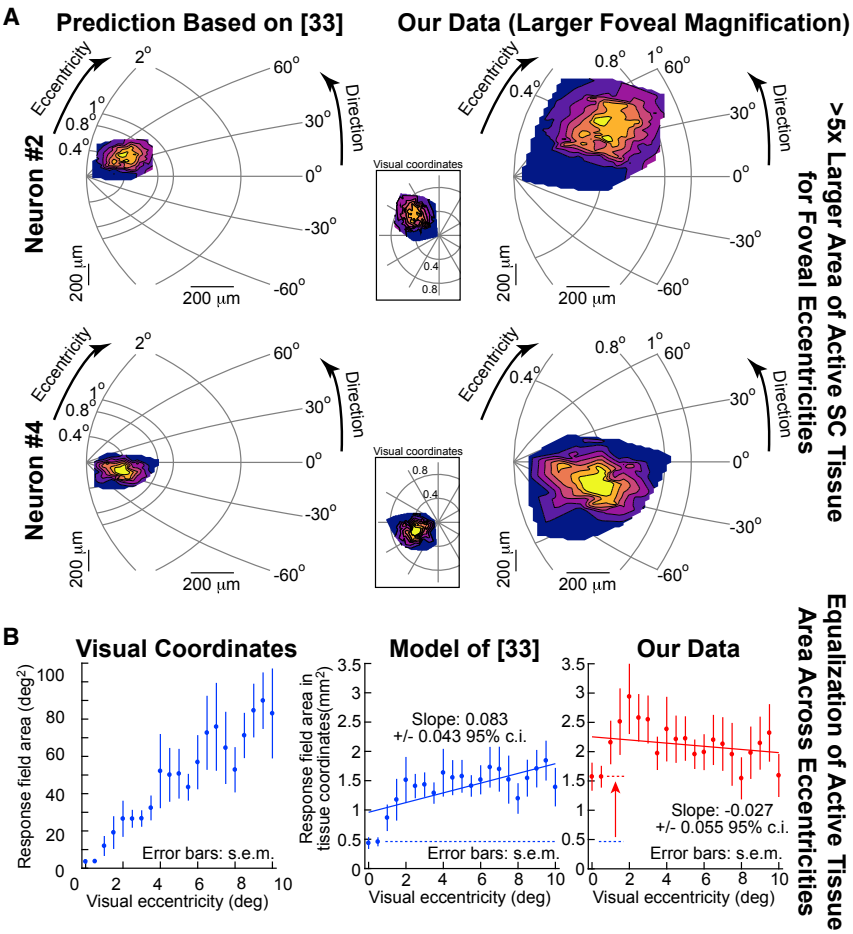

Figure 5. Greater Than Five-Fold Foveal Tissue Area Magnification Than Previously Assumed

(A) Each row shows the projection of an example neuron's visual RF in anatomical coordinates (left: classic SC model; right: our model). This is equivalent to estimating the SC neural tissue area activated by a stimulus [33, 36]. Insets show each neuron's visual RF in visual coordinates. Our topography data (right column) demonstrate larger than five-fold active area for foveal visual locations than the old [33] estimate (left column). We rotated the SC such that the representation of the horizontal meridian is horizontal.

(B) RF areas in visual coordinates from monkeys N and P expectedly increased with eccentricity (leftmost panel). This should be "equalized" in SC neural tissue due to foveal magnification [33, 36]. However, using the classic model [33] fails to result in equalization when foveal neurons are included in analysis (positive slope in middle panel; also: $p = 4.851 \times 10^{-8}$; one-way ANOVA as a function of eccentricity; $F = 4.13$). This failure was also noted in [36]. With larger foveal magnification (rightmost panel; upward red arrow), such equalization is successful (zero slope in rightmost panel; also: $p = 0.025$; one-way ANOVA as a function of eccentricity; $F = 1.77$).

Also see Figure S7.

V1 measurements [11] (Figure 4F; this time plotted as "inverse magnification factor" by the authors of the meta-analysis; that is, min arc of visual eccentricity per mm of neural tissue). SC foveal magnification was as strong as V1 magnification.

An immediate functional implication of large foveal magnification is that foveal light spots would simultaneously activate a large population of neurons. Specifically, because each RF is spatially extended, a single stimulus is expected to activate multiple neurons. For example, for neurons no. 2 and no. 4 from Figure 1, plotting their RF images in neural tissue space revealed that the area occupied in anatomical space was greater than five-fold the area predicted by the classic model of SC topography (Figure 5A, compare right and left columns; the SC was rotated to make the eccentricity dimension horizontal in the figure). This means that a small foveal spot (e.g., at 0.5-degree eccentricity) would activate an area of SC neural tissue greater than five times larger than would be classically predicted [33]. This is significant because a well-known theoretical consequence of foveal magnification is equalization of the size of the active population across eccentricities [33]. With the classic model, plotting RF area versus eccentricity in visual (Figure 5B, left) and tissue (Figure 5B, middle) space revealed that equalization across eccentricities was only partial (the slope of the regression line in Figure 5B, middle was >0); foveal eccentricities were clear outliers. Only with larger foveal magnification factor, revealed by our SC measurements, could we observe complete equalization (Figure 5B, right).

Our observation of larger SC foveal magnification not only clarifies issues related to sensory representation (e.g., Figure 5), but it additionally recasts interpretations of anatomical SC properties. For example, predictions on efferent projections from SC to eventually reach the eye muscles [37] have previously relied on the classic model of SC topography. However, interpretation of the very same data would be very different based on our measurements of magnification (Figure S6).

Fixational Eye Movements Activate up to 1/4–1/3 of SC Neural Tissue by Foveal Stimuli

An additional functional consequence of large foveal magnification is that small eye movements can, by virtue of moving retinal images, cause substantial variations in SC neural activity. This would happen even for tiny ocular drifts. Consider, for example, the scenario in Figure 6A. A foveal RF has a well-defined inner border represented in black (e.g., Figures 1A, 1B, and 2B). A small ipsiversive ocular drift would bring the image of the fixation spot into the RF's inner edge. Thus, even with no visual stimuli, the neuron might still be visually activated by the fixation spot. Indeed, a fraction (22.3%) of our foveal neurons showed variable baseline activity. To demonstrate that this activity was visually driven, we identified 100-ms fixation epochs not containing microsaccades. We then assessed eye position relative to the fixation spot (STAR Methods). Example neuron no. 5 (Figure 6B) had an RF hotspot location of 0.3 degree. We obtained fixation epochs and sorted them based on eye position. We also paired each epoch with simultaneously recorded spike rasters (black ticks). The neuron's baseline activity was strongest when eye

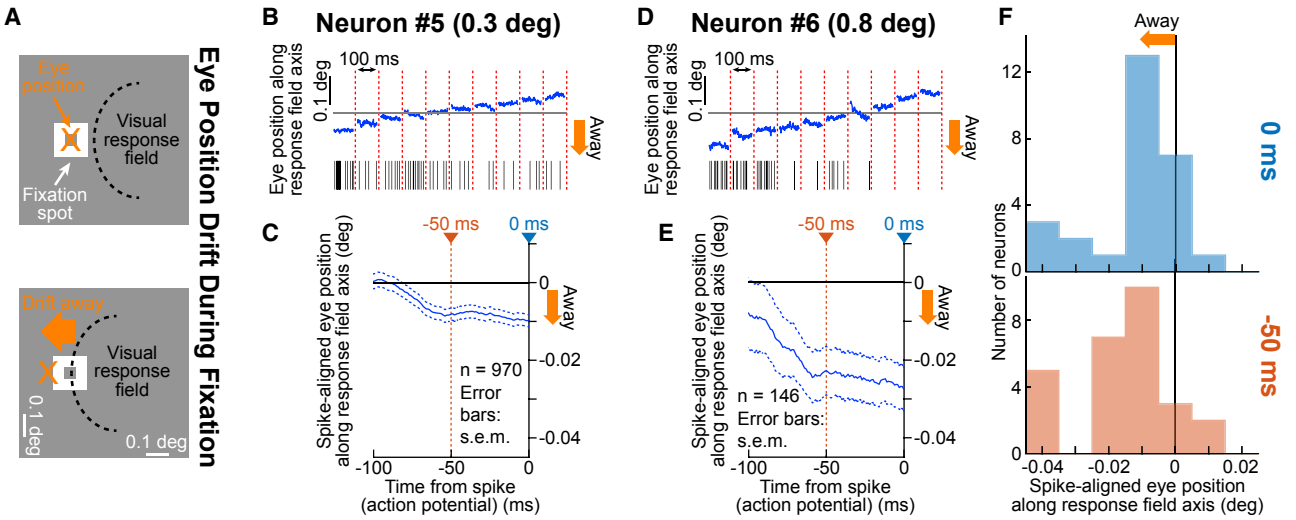

Figure 6. Impact of Ocular Drifts on Foveal Neural Variability

(A) (Top) If gaze (orange) is centered on the fixation spot (white), a foveal RF (black) would not experience visual stimuli. (Bottom) If gaze drifts by <0.1 degree (arrow), the new RF position now experiences the fixation spot as a stimulus.

(B) Example neuron (0.3-degree RF hotspot eccentricity) exhibiting substantial trial-to-trial variability in pre-stimulus activity. We sorted eye position (blue) across trials in microsaccade-free 100-ms epochs (ten example epochs are shown using the conventions of A). Black rasters show corresponding neural activity: highest with eye position farthest away from the fixation spot, consistent with (A).

(C) Spike-triggered average eye position from the same neuron. Spikes were most likely within ~50–100 ms after an eye position deviation away from fixation.

(D) Similar analysis to that in (B) but for a more eccentric neuron. A larger ocular deviation was now needed to cause firing.

(E) This effect is also clear in an analysis of spike-triggered average eye position from the same neuron (similar to C).

(F) For all neurons exhibiting baseline activity, we confirmed (B)–(E) by sampling the value of spike-triggered average eye position at either 0 ms (top histogram) or −50 ms (bottom histogram) relative to spike onset (colored vertical lines in C and E). Spikes were consistently preceded by "away" eye positions (for 0 ms: median = −0.0102, $p = 3.986 \times 10^{-5}$, Wilcoxon signed rank test against 0; for −50 ms: median = −0.0127, $p = 4.422 \times 10^{-5}$, Wilcoxon signed rank test against 0). Also see Figure S7.

position along the axis of the neuron's RF hotspot (similar to Figure 2B analysis) was ipsiversive (bringing the image of the fixation spot into the RF). Thus, trial-to-trial neural variability was related to fixational variability.

We further demonstrated the dependence of neural variability on eye position by computing spike-triggered average eye position leading up to any given spike (Figure 6C). A spike by the neuron was more likely when eye position deviated (up to ~50 ms earlier) away from the fixation spot (along the RF hotspot axis, consistent with the schematic of Figure 6A). Example neuron no. 6 had slightly more eccentric RF preference and was thus activated by larger eye position drifts (Figures 6D and 6E), and measures of spike-triggered eye position were consistent across the population of neurons affording us this analysis (Figure 6F). Therefore, because of foveal representation and magnification, significant variability of ongoing SC activity can be related to fixational gaze behavior.

If one were to now combine the results of Figure 6 with those of Figure 5, it would be possible to estimate, for normal fixational gaze behavior, the amount of SC neural tissue that would be activated simply when normally fixating. This amounts to almost 1/4–1/3 of the entire SC (Figure S7).

Microsaccades Are Associated with Pre-movement Shifts in Foveal SC Representations

Finally, in all of our analyses, we excluded visual onsets near microsaccades because these can alter foveal visual perception [21]. However, we had neurons in which sufficient trials with microsaccades existed, allowing us to investigate a neural basis for such perceptual alteration [21]. We mapped visual RFs without microsaccades and also when stimulus onset occurred <100 ms before microsaccade onset. To avoid contamination by microsaccade-related motor bursts [16], we only considered ipsiversive microsaccades away from RF location and not emitting an ipsiversive microsaccade-related burst. Figures 7A and 7B demonstrate results from two example foveal neurons. Consistent with perceptual alterations [21], both neurons showed an ipsiversive shift in RF hotspot location (i.e., in the same direction as the microsaccade; Figures 7A and 7B rightward component of red arrows) [21]. Across the neurons, there were substantial momentary shifts in RF hotspot locations if stimuli appeared before microsaccades (Figure 7C, left). Interestingly, foveolar neurons always shifted ipsiversively (i.e., in the direction of upcoming microsaccades), whereas more eccentric neurons tended to shift outward; such a reversal is reminiscent of pre-microsaccadic perceptual reversals [21]. Importantly, these RF shifts were not caused by differences in eye positions (Figure 7C, middle and right).

Therefore, there exist not only influences of eye position on SC neural variability due to large foveal magnification (Figures 6 and S7), but microsaccades are also associated with transient changes in SC's foveal representation (Figure 7).

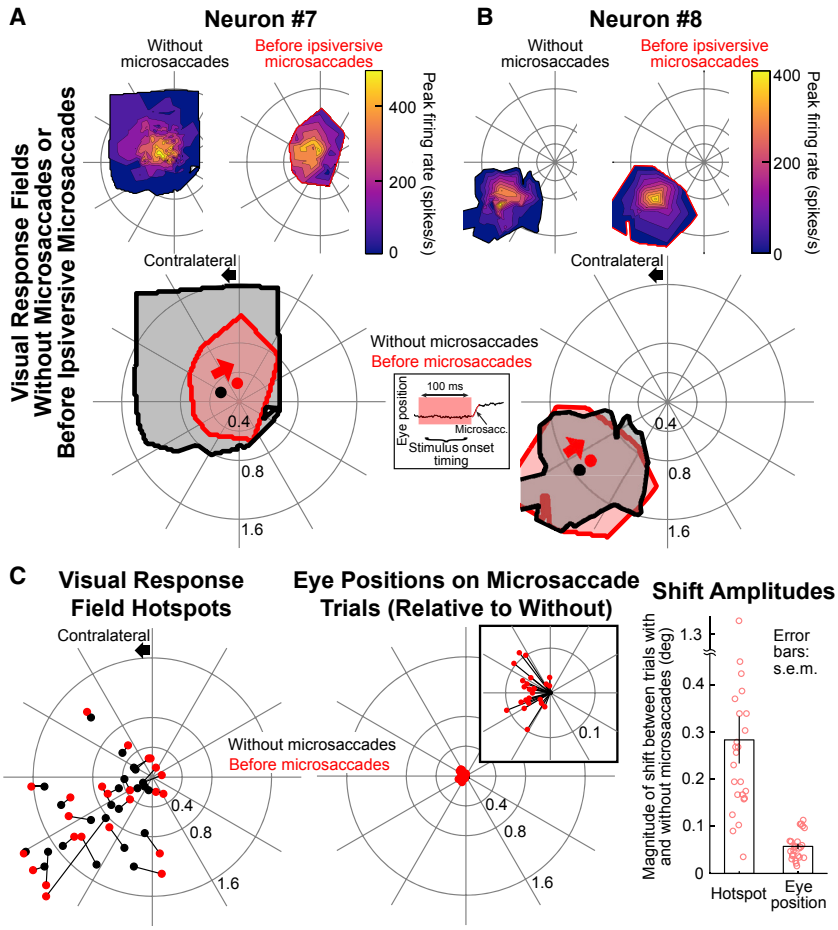

Figure 7. Foveal Visual RFs Shift before Microsaccades

(A) Example neuron mapped with and without microsaccades (STAR Methods). (Top left map) RF without microsaccades is shown. (Top right map) RF obtained with stimuli appearing <100 ms before ipsiversive microsaccades (inset) is shown. The big panel shows RF boundaries and centers from the two conditions. We did not compare RF boundaries because of limited microsaccade numbers. However, the RF hotspot clearly shifted (thick red arrow).

(B) Same as (A) but for another example neuron.

(C) Most foveal neurons exhibited pre-microsaccadic shifts (leftmost plot with black dots being RF hotspot locations without microsaccades and connected red dots being hotspot locations before microsaccades). Because microsaccades alter eye position, we also checked whether the shifts in the left panel could be explained by different eye positions at stimulus onset (middle plot). As expected [15], there was a small shift in eye position before ipsiversive microsaccades (inset in the middle plot), but it was significantly smaller than the RF shifts. The rightmost plot summarizes the magnitude of the RF shifts (left bar) or eye position shifts (right bar) with and without microsaccades. Each circle is a neuron (n = 24). Pre-microsaccadic RF shifts were larger than predicted by eye position shifts ($p = 2.0706 \times 10^{-5}$; Wilcoxon signed rank test).

DISCUSSION

The SC is a phylogenetically old structure linking sensation and action. Its visual machinery in lower animals is critical, and recent results in rodents even suggest that it has dedicated access to cortex [38]. In primates, the SC is historically discussed from the perspective of gaze shifting [39], but it does have visual machinery [9, 23–25, 40–44] capable of both modulating cortical areas [45] and influencing eye movements [23]. Understanding such machinery from the perspective of foveal vision is important. For example, it is generally believed that SC inherits primarily magnocellular visual information [4]. Moreover, debates have existed about whether foveal information is directly routed from retina to SC [5, 41, 46–50], but work since then has become increasingly sparse. Nowadays, a prevailing assumption is that foveal vision is the domain of retino-geniculate pathways, whereas extra-foveal event detection for gaze shifts is the purview of SC [40, 51]. Our results revise this view.

Our findings of large SC foveal magnification are particularly intriguing because they affect the interpretation of a variety of effects related to eye movement control, perception, and cognition. We used the impacts of fixational eye movements on visual stimulus representation (Figures 5, 6, 7, and S7) to highlight an example of this, and we found that SC foveal magnification is similar to that in V1. In hindsight, this makes sense: if the SC is to visually guide precise microsaccadic gaze alignment [16, 30], it ought to also have a high-fidelity visual representation. Moreover, large foveal magnification makes observations of significant influences of small eye movements on peripheral SC visual activity [15] reasonable: although peripheral stimuli are distant in visual coordinates, they are more proximal to foveal SC through magnification. Such influences, if they originate in SC, can also propagate to cortex, given that the SC modulates cortical areas through ascending pathways [45]. Thus, our findings of large foveal magnification are consistent with increasing evidence that active fixational gaze behavior can have far-reaching impacts on neural activity and perception [15, 21].

Large foveal magnification can also be of interest to investigations of SC roles in processes beyond vision, such as decision making and covert selection [52–55]. Moreover, the SC topographic map is frequently invoked to analyze perceptual behavior, both in normal subjects (e.g., [56]) and patients (e.g., [57]). Thus, revising the classic topography model is important. Indeed, in terms of topography, the SC field has essentially been anchored to a single 1972 study [35], based on which the universally accepted model [33] was extrapolated. However, [35] was based on electrically evoked saccades, primarily from extra-foveal sites. Our direct mappings do not require extrapolation into the foveal representation, as in [33], providing a more reliable map (Figure 4). It would be interesting in the future to repeat our dense mappings but for saccade movement fields instead of visual RFs.

Our revised topographic model of SC surface is, therefore, a useful resource for further investigations of structure-function

relationships in the visual and oculomotor systems (Data S1). For simplicity, we formulated the model based on the same mathematical equations as [33], but additional variants may be envisioned, such as including asymmetries in upper visual field representation [25]. Anesthesia and multi-unit recording of the most superficial (retina-recipient) SC laminae in our experiments reduced the chance of observing strong instantiations of these asymmetries in neural RFs. Indeed, our anesthetized superficial RF areas were approximately ten-fold smaller than the awake RFs (Figures 2A, S3A, and S3B). Nonetheless, we do routinely observe magnified foveal representations in all of our awake monkeys (e.g., Figure S5), even beyond monkeys N and P.

Our model, along with the strict lateralization that we observed in both awake and anesthetized animals (e.g., Figure 2), also raises interesting questions on anatomical interactions between the two SCs, for example, along the vertical meridian. Specifically, we found that no visual RFs preferred ipsilateral locations (even near-vertical ones; Figure 1B) and that the inner borders of RFs along the eccentricity dimension were strictly contralateral (Figures 2B and 2C). Both of these observations are different from deeper microsaccade-related responses in the same SC region [17], but they are consistent with a "split fovea" visual representation [46, 58]. Such a representation might appear computationally problematic at face value (creating a visual field discontinuity). However, in reality, we think that fixational eye movements continuously shift images such that the likelihood, at any one moment in time, of a purely vertical stimulus (i.e., along the discontinuity) is very low.

Finally, we found high light sensitivity of foveal SC (Figure 1A). It would be interesting to investigate the implications of such foveal sensitivity on perception and action. It would also be interesting to look at functional cell-type diversity in foveal SC, beyond just characterizing visual responses on the one hand (this study) and deeper microsaccade-related activity [17] and/or goal-representation activity [59] on the other. This is a topic that is beginning to receive attention. For example, in [60], distinct visual-movement response types were reported. The most interesting type is that of neurons bursting during microsaccades only when a visual stimulus was being targeted by these eye movements. Such visual dependence of movement bursts is an SC property that warrants revisiting in much more detail.

STAR★METHODS

Detailed methods are provided in the online version of this paper and include the following:

- KEY RESOURCES TABLE
- CONTACT FOR REAGENT AND RESOURCE SHARING
- EXPERIMENTAL MODEL AND SUBJECT DETAILS
  - Animals used for awake experiments
  - Animals used for anesthetized experiments
  - Animal preparation for awake experiments
  - Animal preparation for anesthetized experiments
- METHOD DETAILS
  - Behavioral tasks for awake experiments
  - Memory-guided saccade task
  - Delayed visually-guided saccade task
  - Fixation visual RF mapping task
- QUANTIFICATION AND STATISTICAL ANALYSIS
  - Statistical tests
  - Neuron classification
  - Visual and motor RF hotspot and area calculations
  - Visual RF skewness
  - Visual response sensitivity and latency
  - Neural modulations during fixational ocular drifts
  - Shifts in visual hotspots prior to microsaccades
  - Estimating a new SC surface topography map
  - Foveal tissue magnification factor
  - Constructing 3-dimensional SC surface topography
- DATA AND SOFTWARE AVAILABILITY
  - Data S1 (separate file)

SUPPLEMENTAL INFORMATION

Supplemental Information can be found online at https://doi.org/10.1016/j.cub.2019.05.040.

ACKNOWLEDGMENTS

We thank H. Korbmacher and E. Brockmann for technical support. C.-Y.C. and Z.M.H. were funded by (1) the Deutsche Forschungsgemeinschaft (DFG, German Research Foundation)—projektnummer 276693517—SFB 1233) and (2) the Werner Reichardt Centre for Integrative Neuroscience (CIN). The CIN is an excellence cluster funded by the DFG (EXC 307). C.D. and K.-P.H. were funded by DFG grant Ho-450/25-1 and by ZEN grant 1.001/09/013 of the Gemeinnuetzige Hertie Foundation.

AUTHOR CONTRIBUTIONS

C.-Y.C., C.D., K.-P.H., and Z.M.H. designed the study. C.-Y.C. and Z.M.H. conducted the awake monkey experiments. C.D. and K.-P.H. conducted the anesthetized monkey experiments. C.D. performed the histology. C.-Y.C., C.D., K.-P.H., and Z.M.H. analyzed the data. Z.M.H. wrote the manuscript. C.-Y.C., C.D., K.-P.H., and Z.M.H. edited the manuscript.

DECLARATION OF INTERESTS

The authors declare no competing interests.

Received: March 26, 2019
Revised: May 1, 2019
Accepted: May 17, 2019
Published: June 27, 2019

REFERENCES

1. Polyak, S.L. (1941). The Retina (University of Chicago Press).
2. Azzopardi, P., and Cowey, A. (1996). The overrepresentation of the fovea and adjacent retina in the striate cortex and dorsal lateral geniculate nucleus of the macaque monkey. Neuroscience *72*, 627–639.
3. Pollack, J.G., and Hickey, T.L. (1979). The distribution of retino-collicular axon terminals in rhesus monkey. J. Comp. Neurol. *185*, 587–602.
4. Schiller, P.H., Malpeli, J.G., and Schein, S.J. (1979). Composition of geniculostriate input ot superior colliculus of the rhesus monkey. J. Neurophysiol. *42*, 1124–1133.
5. Wilson, M.E., and Toyne, M.J. (1970). Retino-tectal and cortico-tectal projections in Macaca mulatta. Brain Res. *24*, 395–406.
6. Curcio, C.A., Sloan, K.R., Jr., Packer, O., Hendrickson, A.E., and Kalina, R.E. (1987). Distribution of cones in human and monkey retina: individual variability and radial asymmetry. Science *236*, 579–582.
7. Rolls, E.T., and Cowey, A. (1970). Topography of the retina and striate cortex and its relationship to visual acuity in rhesus monkeys and squirrel monkeys. Exp. Brain Res. *10*, 298–310.

8. Perry, V.H., and Cowey, A. (1985). The ganglion cell and cone distributions in the monkey's retina: implications for central magnification factors. Vision Res. *25*, 1795–1810.
9. Cynader, M., and Berman, N. (1972). Receptive-field organization of monkey superior colliculus. J. Neurophysiol. *35*, 187–201.
10. Van Essen, D.C., Newsome, W.T., and Maunsell, J.H. (1984). The visual field representation in striate cortex of the macaque monkey: asymmetries, anisotropies, and individual variability. Vision Res. *24*, 429–448.
11. Dow, B.M., Snyder, A.Z., Vautin, R.G., and Bauer, R. (1981). Magnification factor and receptive field size in foveal striate cortex of the monkey. Exp. Brain Res. *44*, 213–228.
12. Polyak, S., and Kluver, H. (1957). The Vertebrate Visual System: Its Origin, Structure, and Function and Its Manifestations in Disease with an Analysis of Its Role in the Life of Animals and in the Origin of Man (University of Chicago Press).
13. McGregor, J.E., Yin, L., Yang, Q., Godat, T., Huynh, K.T., Zhang, J., Williams, D.R., and Merigan, W.H. (2018). Functional architecture of the foveola revealed in the living primate. PLoS ONE *13*, e0207102.
14. Hafed, Z.M. (2011). Mechanisms for generating and compensating for the smallest possible saccades. Eur. J. Neurosci. *33*, 2101–2113.
15. Hafed, Z.M., Chen, C.-Y., and Tian, X. (2015). Vision, perception, and attention through the lens of microsaccades: mechanisms and implications. Front. Syst. Neurosci. *9*, 167.
16. Hafed, Z.M., and Krauzlis, R.J. (2012). Similarity of superior colliculus involvement in microsaccade and saccade generation. J. Neurophysiol. *107*, 1904–1916.
17. Hafed, Z.M., Goffart, L., and Krauzlis, R.J. (2009). A neural mechanism for microsaccade generation in the primate superior colliculus. Science *323*, 940–943.
18. Ko, H.K., Poletti, M., and Rucci, M. (2010). Microsaccades precisely relocate gaze in a high visual acuity task. Nat. Neurosci. *13*, 1549–1553.
19. Guerrasio, L., Quinet, J., Büttner, U., and Goffart, L. (2010). Fastigial oculomotor region and the control of foveation during fixation. J. Neurophysiol. *103*, 1988–2001.
20. Tian, X., Yoshida, M., and Hafed, Z.M. (2018). Dynamics of fixational eye position and microsaccades during spatial cueing: the case of express microsaccades. J. Neurophysiol. *119*, 1962–1980.
21. Hafed, Z.M. (2013). Alteration of visual perception prior to microsaccades. Neuron *77*, 775–786.
22. Andrade da Costa, B.L., and Hokoç, J.N. (2000). Photoreceptor topography of the retina in the New World monkey Cebus apella. Vision Res. *40*, 2395–2409.
23. Chen, C.Y., Sonnenberg, L., Weller, S., Witschel, T., and Hafed, Z.M. (2018). Spatial frequency sensitivity in macaque midbrain. Nat. Commun. *9*, 2852.
24. Chen, C.Y., and Hafed, Z.M. (2018). Orientation and contrast tuning properties and temporal flicker fusion characteristics of primate superior colliculus neurons. Front. Neural Circuits *12*, 58.
25. Hafed, Z.M., and Chen, C.-Y. (2016). Sharper, stronger, faster upper visual field representation in primate superior colliculus. Curr. Biol. *26*, 1647–1658.
26. Marino, R.A., Levy, R., Boehnke, S., White, B.J., Itti, L., and Munoz, D.P. (2012). Linking visual response properties in the superior colliculus to saccade behavior. Eur. J. Neurosci. *35*, 1738–1752.
27. Packer, O., Hendrickson, A.E., and Curcio, C.A. (1989). Photoreceptor topography of the retina in the adult pigtail macaque (Macaca nemestrina). J. Comp. Neurol. *288*, 165–183.
28. Lee, C., Rohrer, W.H., and Sparks, D.L. (1988). Population coding of saccadic eye movements by neurons in the superior colliculus. Nature *332*, 357–360.
29. Freeman, J., and Simoncelli, E.P. (2011). Metamers of the ventral stream. Nat. Neurosci. *14*, 1195–1201.
30. Poletti, M., Listorti, C., and Rucci, M. (2013). Microscopic eye movements compensate for nonhomogeneous vision within the fovea. Curr. Biol. *23*, 1691–1695.
31. Mallot, H.A., von Seelen, W., and Giannakopoulos, F. (1990). Neural mapping and space-variant image processing. Neural Netw. *3*, 245–263.
32. Calabrese, E., Badea, A., Coe, C.L., Lubach, G.R., Shi, Y., Styner, M.A., and Johnson, G.A. (2015). A diffusion tensor MRI atlas of the postmortem rhesus macaque brain. Neuroimage *117*, 408–416.
33. Ottes, F.P., Van Gisbergen, J.A., and Eggermont, J.J. (1986). Visuomotor fields of the superior colliculus: a quantitative model. Vision Res. *26*, 857–873.
34. Daniel, P.M., and Whitteridge, D. (1961). The representation of the visual field on the cerebral cortex in monkeys. J. Physiol. *159*, 203–221.
35. Robinson, D.A. (1972). Eye movements evoked by collicular stimulation in the alert monkey. Vision Res. *12*, 1795–1808.
36. Marino, R.A., Rodgers, C.K., Levy, R., and Munoz, D.P. (2008). Spatial relationships of visuomotor transformations in the superior colliculus map. J. Neurophysiol. *100*, 2564–2576.
37. Grantyn, A., Brandi, A.M., Dubayle, D., Graf, W., Ugolini, G., Hadjidimitrakis, K., and Moschovakis, A. (2002). Density gradients of trans-synaptically labeled collicular neurons after injections of rabies virus in the lateral rectus muscle of the rhesus monkey. J. Comp. Neurol. *451*, 346–361.
38. Beltramo, R., and Scanziani, M. (2019). A collicular visual cortex: neocortical space for an ancient midbrain visual structure. Science *363*, 64–69.
39. Hafed, Z.M. (2018). Superior colliculus: a vision for orienting. Curr. Biol. *28*, R1111–R1113.
40. Schiller, P.H. (1972). The role of the monkey superior colliculus in eye movement and vision. Invest. Ophthalmol. *11*, 451–460.
41. Schiller, P.H., Stryker, M., Cynader, M., and Berman, N. (1974). Response characteristics of single cells in the monkey superior colliculus following ablation or cooling of visual cortex. J. Neurophysiol. *37*, 181–194.
42. Schiller, P.H., and Koerner, F. (1971). Discharge characteristics of single units in superior colliculus of the alert rhesus monkey. J. Neurophysiol. *34*, 920–936.
43. Goldberg, M.E., and Wurtz, R.H. (1972). Activity of superior colliculus in behaving monkey. I. Visual receptive fields of single neurons. J. Neurophysiol. *35*, 542–559.
44. Marrocco, R.T., and Li, R.H. (1977). Monkey superior colliculus: properties of single cells and their afferent inputs. J. Neurophysiol. *40*, 844–860.
45. Berman, R.A., and Wurtz, R.H. (2008). Exploring the pulvinar path to visual cortex. Prog. Brain Res. *171*, 467–473.
46. Cowey, A., and Perry, V.H. (1980). The projection of the fovea to the superior colliculus in rhesus monkeys. Neuroscience *5*, 53–61.
47. Hubel, D.H., LeVay, S., and Wiesel, T.N. (1975). Mode of termination of retinotectal fibers in macaque monkey: an autoradiographic study. Brain Res. *96*, 25–40.
48. Perry, V.H., and Cowey, A. (1984). Retinal ganglion cells that project to the superior colliculus and pretectum in the macaque monkey. Neuroscience *12*, 1125–1137.
49. Hendrickson, A., Wilson, M.E., and Toyne, M.J. (1970). The distribution of optic nerve fibers in Macaca mulatta. Brain Res. *23*, 425–427.
50. Lund, R.D. (1972). Synaptic patterns in the superficial layers of the superior colliculus of the monkey, Macaca mulatta. Exp. Brain Res. *15*, 194–211.
51. Wurtz, R.H., and Mohler, C.W. (1976). Enhancement of visual responses in monkey striate cortex and frontal eye fields. J. Neurophysiol. *39*, 766–772.
52. Crapse, T.B., Lau, H., and Basso, M.A. (2018). A role for the superior colliculus in decision criteria. Neuron *97*, 181–194.e6.
53. Odegaard, B., Grimaldi, P., Cho, S.H., Peters, M.A.K., Lau, H., and Basso, M.A. (2018). Superior colliculus neuronal ensemble activity signals optimal rather than subjective confidence. Proc. Natl. Acad. Sci. USA *115*, E1588–E1597.

54. Grimaldi, P., Cho, S.H., Lau, H., and Basso, M.A. (2018). Superior colliculus signals decisions rather than confidence: analysis of single neurons. J. Neurophysiol. *120*, 2614–2629.
55. Herman, J.P., Katz, L.N., and Krauzlis, R.J. (2018). Midbrain activity can explain perceptual decisions during an attention task. Nat. Neurosci. *21*, 1651–1655.
56. Grujic, N., Brehm, N., Gloge, C., Zhuo, W., and Hafed, Z.M. (2018). Perisaccadic perceptual mislocalization is different for upward saccades. J. Neurophysiol. *120*, 3198–3216.
57. Savina, O., and Guitton, D. (2018). The primitive retino-tecto-reticular pathway is functional in hemidecorticate patients. Curr. Biol. *28*, R1184–R1186.
58. Lavidor, M., and Walsh, V. (2004). The nature of foveal representation. Nat. Rev. Neurosci. *5*, 729–735.
59. Krauzlis, R.J., Basso, M.A., and Wurtz, R.H. (1997). Shared motor error for multiple eye movements. Science *276*, 1693–1695.
60. Willeke, K.-F., Tian, X., Buonocore, A., Bellet, J., Ramirez-Cardenas, A., and Hafed, Z.M. (2019). Memory-guided microsaccades. bioRxiv. https://doi.org/10.1101/539205.
61. Andrey, P., and Maurin, Y. (2005). Free-D: an integrated environment for three-dimensional reconstruction from serial sections. J. Neurosci. Methods *145*, 233–244.
62. Yushkevich, P.A., Piven, J., Hazlett, H.C., Smith, R.G., Ho, S., Gee, J.C., and Gerig, G. (2006). User-guided 3D active contour segmentation of anatomical structures: significantly improved efficiency and reliability. Neuroimage *31*, 1116–1128.
63. Chen, C.Y., and Hafed, Z.M. (2013). Postmicrosaccadic enhancement of slow eye movements. J. Neurosci. *33*, 5375–5386.
64. Chen, C.Y., Ignashchenkova, A., Thier, P., and Hafed, Z.M. (2015). Neuronal response gain enhancement prior to microsaccades. Curr. Biol. *25*, 2065–2074.
65. Chen, C.Y., and Hafed, Z.M. (2017). A neural locus for spatial-frequency specific saccadic suppression in visual-motor neurons of the primate superior colliculus. J. Neurophysiol. *117*, 1657–1673.
66. Fuchs, A.F., and Robinson, D.A. (1966). A method for measuring horizontal and vertical eye movement chronically in the monkey. J. Appl. Physiol. *21*, 1068–1070.
67. Judge, S.J., Richmond, B.J., and Chu, F.C. (1980). Implantation of magnetic search coils for measurement of eye position: an improved method. Vision Res. *20*, 535–538.
68. Distler, C., and Hoffmann, K.P. (2001). Cortical input to the nucleus of the optic tract and dorsal terminal nucleus (NOT-DTN) in macaques: a retrograde tracing study. Cereb. Cortex *11*, 572–580.
69. Hoffmann, K.P., Bremmer, F., Thiele, A., and Distler, C. (2002). Directional asymmetry of neurons in cortical areas MT and MST projecting to the NOT-DTN in macaques. J. Neurophysiol. *87*, 2113–2123.
70. Tian, X., Yoshida, M., and Hafed, Z.M. (2016). A microsaccadic account of attentional capture and inhibition of return in Posner cueing. Front. Syst. Neurosci. *10*, 23.
71. Buonocore, A., Chen, C.Y., Tian, X., Idrees, S., Münch, T.A., and Hafed, Z.M. (2017). Alteration of the microsaccadic velocity-amplitude main sequence relationship after visual transients: implications for models of saccade control. J. Neurophysiol. *117*, 1894–1910.
72. Mohler, C.W., and Wurtz, R.H. (1976). Organization of monkey superior colliculus: intermediate layer cells discharging before eye movements. J. Neurophysiol. *39*, 722–744.
73. Barlow, H.B., Blakemore, C., and Pettigrew, J.D. (1967). The neural mechanism of binocular depth discrimination. J. Physiol. *193*, 327–342.
74. Illing, R.B. (1988). Spatial relation of the acetylcholinesterase-rich domain to the visual topography in the feline superior colliculus. Exp. Brain Res. *73*, 589–594.
75. Seligman, A.M., Karnovsky, M.J., Wasserkrug, H.L., and Hanker, J.S. (1968). Nondroplet ultrastructural demonstration of cytochrome oxidase activity with a polymerizing osmiophilic reagent, diaminobenzidine (DAB). J. Cell Biol. *38*, 1–14.
76. Humphrey, N.K. (1968). Responses to visual stimuli of units in the superior colliculus of rats and monkeys. Exp. Neurol. *20*, 312–340.
77. Wurtz, R.H., and Albano, J.E. (1980). Visual-motor function of the primate superior colliculus. Annu. Rev. Neurosci. *3*, 189–226.
78. Munoz, D.P., and Wurtz, R.H. (1995). Saccade-related activity in monkey superior colliculus. I. Characteristics of burst and buildup cells. J. Neurophysiol. *73*, 2313–2333.
79. Gur, M., and Snodderly, D.M. (2006). High response reliability of neurons in primary visual cortex (V1) of alert, trained monkeys. Cereb. Cortex *16*, 888–895.
80. Tang, Y., Saul, A., Gur, M., Goei, S., Wong, E., Ersoy, B., and Snodderly, D.M. (2007). Eye position compensation improves estimates of response magnitude and receptive field geometry in alert monkeys. J. Neurophysiol. *97*, 3439–3448.
81. Haider, B., Häusser, M., and Carandini, M. (2013). Inhibition dominates sensory responses in the awake cortex. Nature *493*, 97–100.
82. Vaiceliunaite, A., Erisken, S., Franzen, F., Katzner, S., and Busse, L. (2013). Spatial integration in mouse primary visual cortex. J. Neurophysiol. *110*, 964–972.
83. Caliński, T., and Harabasz, J. (1974). A dendrite method for cluster analysis. Commun. Statist. *3*, 1–27.
84. Legéndy, C.R., and Salcman, M. (1985). Bursts and recurrences of bursts in the spike trains of spontaneously active striate cortex neurons. J. Neurophysiol. *53*, 926–939.
85. Munoz, D.P., and Wurtz, R.H. (1995). Saccade-related activity in monkey superior colliculus. II. Spread of activity during saccades. J. Neurophysiol. *73*, 2334–2348.

STAR★METHODS

KEY RESOURCES TABLE

REAGENT or RESOURCE	SOURCE	IDENTIFIER
Software and Algorithms		
MATLAB	The MathWorks, Inc.	https://www.mathworks.com/products/matlab.html; RRID: SCR_001622
Free-D	[61]	http://free-d.versailles.inra.fr/; RRID: SCR_009578
ITK-SNAP	[62]	http://www.itksnap.org/pmwiki/pmwiki.php; RRID: SCR_002010

CONTACT FOR REAGENT AND RESOURCE SHARING

Further information and requests for resources should be directed to and will be fulfilled by the Lead Contact, Ziad M. Hafed (ziad.m.hafed@cin.uni-tuebingen.de).

EXPERIMENTAL MODEL AND SUBJECT DETAILS

Animals used for awake experiments

Two male macaque monkeys (*Macaca mulatta*), aged 7 years and weighing 7-10 kg.

Animals used for anesthetized experiments

Two male macaque monkeys (one *Macaca fascicularis* and one *Macaca mulatta*). The *Macaca fasicularis* monkey (monkey F) was aged 13 years and weighed 6.3 kg. The *Macaca mulatta* monkey (monkey R) was aged 6 years and weighed 7 kg.

Animal preparation for awake experiments

Macaque monkeys N and P (male, *Macaca mulatta*, aged 7 years and weighing 7-10 kg) were prepared earlier [25, 63–65]. Briefly, we surgically attached a titanium head holder to each monkey's skull with titanium skull screws. The head holder was used for stabilizing head position during experiments. After recovery and initial behavioral training, we implanted a scleral search coil in one eye to allow eye movement measurement using the magnetic induction technique [66, 67]. For neural recordings from superior colliculus (SC), we implanted recording chambers, placed on the midline with chamber center being aimed at a point 1 mm posterior of and 15 mm above the interaural line [64]. The chambers were tilted backward from vertical by 35 deg in monkey N and 38 deg in monkey P.

All experiments were approved by ethics committees at the regional governmental offices of the city of Tübingen (Regierungspräsidium Tübingen), and they were in accordance with European Union directives on animal research, along with the German governmental implementations of these directives.

Animal preparation for anesthetized experiments

Two male macaque monkeys (monkey F, *Macaca fascicularis*, aged 13 years, weighing 6.3 kg; monkey R, *Macaca mulatta*, aged 6 years, weighing 7 kg) were used. Both monkeys had also taken part in other projects [68, 69]. In particular, in monkey F, the right and left nucleus of the optic tract (NOT) were injected with retrograde tracer a few days before the present experiments, but the injections were small, and we did not notice any appreciable effects on SC visual RF properties from them. In monkey R, the left SC (opposite to the one that we mapped) as well as the left NOT also received tracer injections a few days before the present experiments. All experiments were approved by the local authorities (Regierungspräsidium Arnsberg, now LANUV) and ethics committee, and they were performed in accordance with the Deutsche Tierschutzgesetz of 7.26.2002, the European Communities Council Directive RL 2010/63/EC, and NIH guidelines for care and use of animals for experimental procedures.

The animals were pre-medicated with 0.04 mg/kg atropine and initially anesthetized with 10 mg/kg ketamine hydrochloride i.m. (Braun, Melsungen, Germany). After local anesthesia with 10% xylocain (Astra Zeneka, Wedel), they were intubated through the mouth, and an intravenous catheter was placed into the saphenous vein. After additional local anesthesia of their auditory canals and the skin above the planned craniotomy with bupivacain hydrochloride 0.5% (Bupivacain ®, DeltaSelect, Pfullingen, Germany) or prilocainhydrochloride 0.5% (Xylonest®, Astra Zeneca, Wedel, Germany), the animals were placed into a stereotaxic apparatus and artificially ventilated with a nitrous oxide:oxygen ratio of 3:1. Ventilation also contained 0.3%–1% halothane as needed according to no change in heart rate during algetic stimuli (1% during surgery, 0.3%–0.5% during recording). The skin overlying the skull was cut, and a craniotomy was performed to allow access to the SC, either vertically from above (monkey R) or at an angle of 45 deg posterior (monkey F). Heart rate, SPO_2, blood pressure, body temperature, and end-tidal CO_2 were monitored constantly and maintained at physiological values. Corneae were protected with contact lenses chosen with a refractometer (Rodenstock®) to focus the

animals' eyes on the projection screen. After surgery completion, the animals were paralyzed with alcuronium chloride (Alloferin®, MedaPharma, Germany).

METHOD DETAILS

Behavioral tasks for awake experiments

Monkey N and P were trained to maintain precise gaze fixation on a small spot measuring 8.5x8.5 min arc [63]. The same animals were extensively trained on precise fixation and were used in previous studies demonstrating their high oculomotor control capabilities [20, 63, 65, 70, 71]. The fixation spot was a white square (72 Cd/m^2) presented over a gray background (21 Cd/m^2) [25, 64]. Within a given recording session, we isolated individual neurons online (ensuring high signal to noise ratio; Figure S1A) and characterized them using a variety of behavioral tasks. If the monkey was still interested in continuing after a neuron was recorded, we moved the recording electrode deeper into the SC and isolated additional neurons (e.g., Figure S4). We recorded between 1 and 6 neurons per session. The behavioral tasks were chosen in part to classify neuron types and in part to characterize foveal visual neuron response properties as in the main text.

Memory-guided saccade task

This task was used to assist in classifying neurons as possessing a saccade-related movement response independent of visual stimulation [72] (see Neuron classification below). A fixation spot was presented for 300-1000 ms. After the monkey established gaze fixation, a second spot (of the same dimensions) was flashed for ~50 ms and disappeared. The monkey had to maintain fixation and remember the flash location. The fixation spot was then removed after 300-1100 ms; the monkey was trained to generate a saccade to the memorized flash location, and then hold gaze at that location (to within a tolerance window dependent on flash eccentricity) for ~300-500 ms before being rewarded. Liquid reward was given if all trial epochs were successfully completed. Flash location was chosen to be at the response field (RF) hotspot of the isolated neuron, which we estimated from the other visual and saccade tasks described below. We collected > 35 trials from each neuron. If the neuron elicited a saccade-related response, it was classified as being a movement-related neuron that was independent of visual stimulation [72] (see Neuron classification below). We collected data from 271 neurons in this task.

Delayed visually-guided saccade task

This task was used to map visual and saccade-related RF's. A fixation spot was presented for 300-1000 ms. After the monkey established fixation, a second spot (target) was presented. The second spot was the same size as the fixation spot, and its center could be placed as near as ~0.046 deg from the center of the fixation spot in either the horizontal or vertical direction. When the fixation spot was removed 500-1000 ms later, the monkey made a saccade to the target. We varied target location from trial to trial in order to map each neuron's visual and saccade-related RF's. For each neuron, we collected 88 ± 34 s.d. trials. We collected data from 332 neurons in this task. Some of these neurons (primarily the peripheral ones) were used in earlier studies for other purposes [23–25], and they were important here as a suitable reference for comparing, in the same animals, foveal neural response properties.

Fixation visual RF mapping task

For the most foveal neurons, we simplified the delayed visually-guided saccade task. A fixation spot was first presented for 300 −1000 ms. After the monkey established fixation, a second spot was then presented for 250 ms while the monkey maintained fixation. Reward was only contingent on maintaining gaze position at the fixation spot until trial end. We used this task instead of the delayed visually-guided saccade task if the neuron's RF was too close to the fixation spot, making it difficult to instruct a delayed saccade task. Because microsaccades were inevitable in this task, this task still allowed us to explore saccade-related movement fields as well as visual RF's, so the task was conceptually comparable to the delayed visually-guided saccade task. For each isolated neuron, we collected 122 ± 87 s.d. trials. We collected data from 81 neurons in this task.

Visual stimulation in the anesthetized monkeys

We used small spots of light moved across the screen using a hand-held lamp or laser pointer. The laser spots subtended 0.3 cm, or 2 min arc at the screen distance that we used for foveal RF's (570 cm). Single and multi-unit activity was recorded from the SC surface (upper superficial layer), and RF location and extent were determined by moving the stimulus in various directions and at various speeds across a tangent screen at a distance from the eye of 285 cm for peripheral RF's and 570 cm for foveal RF's. To ensure that paralysis was maintained during the experiment, a recording electrode was inserted into the visual cortex (V1) and the RF determined and checked at regular intervals during the entire recording session (also see Visual and motor RF hotspot and area calculations below). Horizontal RF borders were determined online by moving the stimulus up and down starting outside the RF and then shifting it toward RF center. The same procedure, similar to the minimal response field method of [73], was also used for determining the vertical borders (this time with horizontal stimulus movements). The experimenter judged the borders of the RF by listening to an increase in the neural activity.

The exact locations of the horizontal and vertical receptive field borders in degrees of visual angle with respect to the eye contralateral to the recorded SC were measured by use of a laser pointer attached to a 2D angle meter. Two calibrated rotary potentiometers aligned with the position where the eye had been during recording allowed direct reading of the azimuth and elevation values in deg.

Histology (monkeys R and F)

Monkeys N and P are still being used for experiments. Monkeys R and F were sacrificed to reconstruct a 3-dimensional model of superficial SC surface topography (Figures 3, 4, 5, and S7). At the end of the experiments, the animals received a lethal dose of pentobarbital (80-100 mg/kg), and they were perfused through the heart with 0.9% NaCl with 0.1% procaine hydrochloride followed by paraformaldehyde-lysine-periodate containing 4% paraformaldehyde. After postfixating the tissue overnight, it was cryoprotected with 10% and 20% glycerol in 0.1 molar phosphate buffer (pH 7.4) and then flash frozen in isopentane and stored at -70°C.

Frozen sections through the midbrain were cut at 40 μm in the frontal plane (monkey R) or at 50 μm in a plane perpendicular to the SC surface (monkey F). To visualize recording sites and tracer injections [68], alternate series were used for Nissl stain, acetylcholine esterase (AChE) [74] histochemistry, cytochrome C oxidase histochemistry [75], myeloarchitecture, and tracer protocols [68]. The histological sections were photographed by a photomicroscope (Zeiss Axioplan) equipped with a Canon EOS 600D camera. Brightness and contrast were adjusted with Adobe Photoshop (RRID: SciRes_000161, version 5.5).

QUANTIFICATION AND STATISTICAL ANALYSIS

Statistical tests

All results of statistical tests are reported in Results and the appropriate figure legends.

Neuron classification

For the anesthetized monkeys R and F, we recorded only the most superficial SC neurons. These are purely visual [42, 76], also receiving direct retinal projections [3–5]. Therefore, no further classification was done. Neurons encountered at the rostro-lateral border of the SC were assigned to the NOT if they responded in a direction-selective manner to temporo-nasal movement of large area random dot stimuli. Neurons at the caudal border of the SC were localized in the inferior colliculus if they responded to auditory stimuli (hand clapping, whistling, or clicks).

For the awake monkeys N and P, we classified neurons as being purely visual, visual-motor (saccade-related), or purely motor (saccade-related) [25, 64]. We classified a neuron as being visually responsive if average neural activity 0-200 ms after target onset in the delayed visually guided-saccade task or the fixation visual RF mapping task was higher than average neural activity 0-200 ms before target onset (baseline activity) ($p < 0.05$, paired t test.) [25, 64]. We also classified a neuron as being motor responsive if average neural activity 0-50 ms before saccade onset in the delayed visually-guided saccade task or the memory-guided saccade task was higher than average neural activity 100-175 ms before saccade [25, 64].

For some neurons, because the RF of the neuron was very close to fixation, the saccadic tasks were deemed at times to be too demanding for the monkeys. In these cases, we collected microsaccades after fixation spot onset but before the second spot onset from fixation visual RF mapping task. We classified the neurons as being motor responsive by applying the same measurement intervals above but now aligned to contraversive microsaccade onset. We did this for the neurons in which we knew there was no saccade-related response for larger movements.

In total, we analyzed data from 413 neurons from both the right and left SC (162 purely visual, 239 both visually and motor responsive, and 12 purely motor). We often combined purely visual and visual-motor neurons (401 neurons) when analyzing visual response properties, unless a specific difference was noted (e.g., Figure S2C). We were least interested in purely motor neurons because this was not the focus in our study. Microsaccade-related responses were previously described in the SC [16, 17], and we used motor responses in the present study to confirm expected vertical organization of visual, visual-motor, and purely motor neurons across the depths of the SC [77, 78] (e.g., Figure S4).

Visual and motor RF hotspot and area calculations

Because foveal RF's are extremely small (e.g., Figure 1), even the smallest fixational eye movements can smear stimulus position on the retina and therefore alter estimates of RF hotspot location and area [79, 80]. We therefore carefully accounted for eye movement measurements in all of our experiments.

For the anesthetized animals (monkeys R and F), we used a reference electrode placed in the foveal representation of the primary visual cortex (V1) to ensure that there were no eye movements during stimulus presentation for the SC experiments; we ensured that the foveal V1 neuron was regularly stimulated (visually) after we mapped SC RF's. Because we analyzed the entire SC surface topography estimation in a given monkey during a single session with many successive penetrations, we were severely limited in time. We therefore estimated SC RF area by listening to single or multi-unit activity, and we plotted the RF assuming a rectangular shape (e.g., inset in Figure S3A) [73]. We estimated one RF per penetration site in the SC. We demarcated the inner and outer RF locations both horizontally and vertically. Because anesthesia potentially alters RF sizes and neural response properties [81, 82], and because our RF area estimates under anesthesia were less quantitative than the awake monkey procedures described below, we did not perform quantitative comparisons between RF areas in the anesthetized and awake animals. However, we did confirm similar non-uniform sampling of visual space even within the foveola region in both anesthetized and awake animals (e.g., Figures 2A, S3A, and S3B). For example, both anesthetized and awake animals showed a similar approximately ten-fold increase in RF area from fovea to 10 deg of eccentricity.

For the awake monkeys (N and P), we first calibrated eye tracker measurements similar to how we calibrate them in our laboratory (and in the same animals) for our real-time gaze-contingent stimulus presentation experiments [20, 63, 70]. We then corrected for a small technical artifact in the magnetic induction eye coil system that happened in a minority of our sessions. Specifically, for a typical ~6-hour recording session, we sometimes observed a small, abrupt jump in eye position using the eye coil system midway through a session. We confirmed that this was a measurement artifact and not a genuine shift in the monkeys' eye position by performing eye movement analyses (e.g., Figure 6) and also by comparing our strong RF skewness effects (e.g., Figure 2B) with and without artifact correction. For monkey N, we also investigated this artifact in more detail by measuring eye position using both a video-based eye tracker (EyeLink 1000, SR Research, Toronto, Canada) and the magnetic induction eye coil system simultaneously [63]. We corrected this artifact using the following procedure. We measured average eye position 0-50 ms before stimulus onset in a given task in which a potential artifact was suspected (i.e., at the end of the initial fixation interval while the monkeys maintained stable fixation). We excluded trials with microsaccade within 0-100 ms before stimulus onset. We then used a Calinski-Harabasz criterion [83] on horizontal eye position, vertical eye position, and trial sequence to find an optimal clustering number, and we then ran a k-means clustering algorithm using the optimal clustering number. We validated the result by manually observing all clustering results. From among all neurons, 300 contained only 1 cluster (no artifact), and 89 contained 2 clusters. Only 24 neurons had 3 or more clusters. For the multi-cluster files, we corrected the artifact by shifting the displaced clusters to the centroid of the main eye position cloud.

With technical calibration now corrected, we were now in a position to estimate RF properties. For estimating the visual RF area, we excluded all trials containing microsaccades within ± 100 ms around stimulus onset time. We then measured peak firing rate 30-150 ms after stimulus onset. We related this visual response property to retinotopic stimulus location in order to estimate RF area in retinotopic coordinates. We obtained retinotopic stimulus location by accounting for fixational eye position variation across time and trials [20, 70]. Specifically, we measured average eye position 0-50 ms before stimulus onset and related it to the calibrated eye position. We then shifted the true stimulus location in physical display coordinates to the retinotopic location relative to the center of gaze. For example, if the stimulus was physically presented at 15 min arc to the right of the fixation spot on the display, but the eye position at stimulus onset was shifted by 5 min arc to the left of calibrated eye position, then the stimulus location in retinotopic coordinates was in reality at 20 min arc to the right of the center of gaze. Across all stimulus locations and peak firing rate measurements, we used Delaunay triangulation and linearly interpolated the firing rate measurements to obtain a 3-dimensional surface of visual response strength as a function of 2-dimensional stimulus location. We further applied a threshold to accept a location as being within a given RF. The threshold was that the visual response had to be > 3 s.d. above baseline pre-stimulus firing rate during fixation. All locations with visual responses above this threshold were considered to be within the visual RF of a given neuron, and RF hotspot location was the location eliciting the strongest visual response in the triangulated surface. This procedure gave us a more accurate estimate of the RF area and shape, especially when the neurons were extremely close to the fovea (e.g., Figure 2B, left panel), and we confirmed that eye position correction resulted in smaller RF's than without correction [79, 80]. For example, across all neurons (including eccentric ones), the average RF area decreased by 4.2 percent after correction for eye movements.

We used a similar procedure to estimate saccade-related motor RF's. In this case, we measured average firing rate 0-50 ms before saccade onset, and we used saccadic horizontal and vertical eye position deviations as the locations against which we plotted saccade-related firing rate.

In summary analyses (e.g., Figures 2A, S3A, and S3C), we binned eccentricities into 0.25 deg bin widths and used a running window of 0.5 deg step size. In Figure 5B, for visualizing a larger eccentricity range, we used 0.5 deg bin widths and a running window of 1.5 deg step size.

Visual RF skewness

To estimate visual RF skewness along radial retinotopic eccentricity (e.g., Figures 2B and 2C), we plotted a 1-dimensional RF profile: we plotted visual response strength as a function of radial retinotopic eccentricity along the line connecting the center of gaze to the RF hotspot. To compare neurons, we normalized each neuron's 1-dimensional RF profile along eccentricity by the neuron's response at the peak hotspot location. We then combined neurons having a similar preferred retinotopic eccentricities (e.g., Figure 2B). For population statistics of skewness, we fit each neuron's 1-dimensional RF profile as a function of radial eccentricity to a β function, and we acquired the α and β parameters of the fit. These allowed us to estimate the near and far ratios (*a*-to-*b* ratios in Figure 2C) of the RF. We reasoned that this approach of fitting was a more unbiased method for evaluating RF skewness because the mapping could sometimes be incomplete close to the far edge of the RF; fitting takes into account the entire measurement for estimating *a*-to-*b* ratios. We also felt that the fitting gives a direct quantitative measure of RF skewness, but the skewness is also very evident in raw traces as well (Figure 2B, left panel).

To further evaluate the above method, for the same neurons included in the current analysis, we also took another 1-dimensional RF profile, but this time as a function of direction from horizontal along the radial eccentricity of the RF hotspot (e.g., *c*-to-*d* ratio in Figure 2C). The prediction would be that the ratio of the α and β parameters in the beta function fit would now be close to 1 because the asymmetry that we observed in RF's was only observed along the radial dimension (Figures 2B and 2C). In Figure 2C, all neurons with preferred visual eccentricity < 2 deg were analyzed, except for 6 neurons. These neurons were excluded because the RF data fit to a β function did not result in > 80% explained variance by the fit.

Visual response sensitivity and latency

In Figure S2B, we used the highest visual response within a neuron's RF (i.e., at the RF hotspot) as the preferred eccentricity of each neuron. We then binned eccentricities into 0.25 deg bin widths, and we used a running window of 0.5 deg step size, to plot visual sensitivity as a function of preferred eccentricity. We combined neurons from different depths below SC surface because we did not find any significant difference in SC visual response sensitivity across depth from the SC surface. For example, comparing visual sensitivity of neurons with < 1000 μm depth below SC surface to visual sensitivity of neurons with 1000-2000 μm depth resulted in a non-significant effect (Ranksum test, $p = 0.90848$, all neurons preferring < 2 deg eccentricity).

To estimate a neuron's response latency, we first applied Poisson spike train analysis to find the first spike occurring in response to stimulus onset for each trial [23–25, 84]. This method was particularly suitable when a neuron had an ongoing baseline firing rate on which a stimulus-evoked response rode; the method also trivially detected first-spike latency when there was no baseline rate before stimulus onset (e.g., Neurons #1-#4 in Figure 1). To ensure that we were estimating first-spike latency for optimal stimuli across neurons, we estimated each neuron's response latency by averaging first-spike latency only from trials in which the stimulus was near the RF hotspot (i.e., evoking a response larger than half of the peak visual response within a neuron's RF; typically > 22 trials). After we estimated each neuron's response latency for the optimal stimulus location, we plotted the response latency across neural preferred eccentricity using 0.25 deg bin widths and a running window step size of 1 deg. We separated superficial (< 1000 μm below SC surface) and deeper (1000-2000 μm below SC surface) neurons in this analysis because we observed a difference in how response latency depended on eccentricity within foveal space (< 2 deg) as a function of neural depth below SC surface (Figure S2C).

Neural modulations during fixational ocular drifts

To demonstrate that tiny fixational eye movements can have a significant influence on neural variability in the foveal representation, even when no stimuli are presented on the display except for a fixation spot, we identified neurons having a baseline firing rate during fixation (Figure 6). This was done to ensure that we could observe modulations in this baseline activity (i.e., increases or decreases) as a function of eye position. We further only considered trials in which there were no microsaccades for at least 100 ms before stimulus onset (i.e., at the end of the baseline fixation period). In these trials, the only stimulus on the display was the fixation spot (Figure 6A); our goal was to investigate whether drifts of the image of the fixation spot into and out of a foveal neuron's visual RF (because of fixational eye movements) would be sensed by the neurons.

We analyzed eye movements along the axis connecting the center of gaze to the RF hotspot location; that is, we rotated the eye position and RF data based on each neuron's RF hotspot location such that the RF hotspot in the new coordinate reference frame was always to the right of the center of gaze (Figure 6A). This allowed us to investigate eye position variation to or away from the RF (because after rotation, the horizontal eye position change was going to move the fixation spot in or out of the RF, the vertical eye position component was orthogonal to the RF and was less relevant for this analysis; we therefore excluded it from analysis for simplicity).

Next, we filtered our neurons to those having RF hotspot locations being < 1 deg in eccentricity and also firing > 50 spikes in the final 100 ms before stimulus onset. The latter criterion allowed us to have a more sensitive analysis for this particular question that we were interested in addressing (i.e., to observe modulations in this baseline activity by eye position). We also excluded neurons with microsaccades in the critical analysis period. This resulted in 27 neurons for this analysis.

Across trials, we sorted microsaccade-free eye positions based on whether they brought the fixation spot toward the RF border (Figure 6B, top, "Away" eye positions) or away from it. If the neuron was sensitive to the influence of ocular drift on retinal images, then more action potentials should be triggered whenever the image of the fixation spot was brought toward the RF location (Figures 6B and 6C, top). To plot spike-aligned eye position (Figures 6B and 6C, bottom), we took every neural action potential (spike) in the final 100 ms of fixation before stimulus onset, and we plotted the average eye position (along the RF axis) leading up to this action potential. We then averaged all spike-aligned eye positions. Relatively speaking, more eccentric neurons should require larger eye position variation to trigger response variability than less eccentric neurons (e.g., Neurons #6 and #5, respectively, in Figures 6B and 6C).

Shifts in visual hotspots prior to microsaccades

To analyze the impacts of the second type of fixational eye movement that can take place (microsaccades) on foveal visual representations in the SC, we searched for neurons in our database having sufficient numbers of trials satisfying the following criteria. First, stimulus onset had to occur before microsaccades (within 100 ms), such that we can analyze evoked responses even before a shift in eye position had taken place. Second, there had to be sufficient trials to allow estimating a map of the RF (> 10 trials within the RF region). Third, the microsaccades had to be directed opposite the hemifield represented by the SC side that we were recording from, so that we could avoid observing microsaccade-related elevations in firing rate [17], which can mask visually-evoked responses by stimulus onset. Fourth, the neurons had to show no microsaccade-related movement burst for these ipsiversive microsaccades. Finally, the neurons had to have RF hotspot locations < 2 deg in eccentricity. We then reconstructed visual RF maps without microsaccades (as in all of our analyses) or when stimuli appeared in pre-microsaccadic intervals. Since these intervals are associated with perceptual mislocalizations in the fovea [21], we analyzed whether RF hotspot locations were shifted by amounts larger than predicted by simple shifts in eye position caused by the microsaccades themselves. Because all of our calibrations in eye position were done for microsaccade-free fixation (see Visual and motor RF hotspot and area calculations above), we also confirmed that

eye position shifts caused by microsaccades in the present analysis were insufficient to explain our results (e.g., Figure 7C). We included 24 neurons in this analysis; on average, we had 22 ± 15.3 s.d. trials for each neuron with microsaccades.

Estimating a new SC surface topography map

The universally accepted map of SC topography [33] was based on peripheral measurements of electrically-evoked saccades from [35]. We used a similar approach to [35], but now densely mapping the most superficial SC laminae in monkeys R and F and with visual stimuli as opposed to electrical microstimulation of the deeper saccade-related layers. We also made sure to measure both peripheral and foveal sites such that no extrapolation into the fovea (from peripheral-only measurements) is necessary.

We mapped the left SC of monkey F using 500 μm resolution, and using a penetration angle tilted 45 deg posterior of vertical. In monkey R, we mapped the right SC surface topography using 250 μm resolution and vertical penetrations. During the mappings, we also physiologically determined the SC borders, by identifying neighboring sites (Figure 3A). We performed 91 penetrations, ranging from 0.1 to 49 deg in eccentricity in monkey F, and 124 penetrations, ranging from 0.04 to 12 deg in monkey R. In order to align the SC from the two monkeys, and to obtain a direct comparison to [33], we projected monkey R's recordings into the same 45 deg posterior of vertical coordinate frame (like monkey F). We did this because the original peripheral SC mappings [35], based on which the universally accepted SC topography map [33] was obtained, were performed using the same approach.

We then ran a rigid body transformation to align recording sites from the two monkeys. In the visual region of overlap between the two monkeys (up to 12 deg eccentricity), we minimized the least-mean-square error between the preferred eccentricity and visual angles of SC sites from the two monkeys. This allowed co-registration of the two SC's. We validated this co-registration by plotting the non-SC locations that we physiologically measured during the experiments. We confirmed that none of the non-SC sites after co-registration encroached on our aligned SC sites. We also confirmed that there was good agreement in the non-SC sites with known anatomical geometry relative to SC location (e.g., pretectum or cerebellum), and that our map was even consistent with 3-dimensional anatomy of the SC (see Constructing 3-dimensional SC topography below). The results of the final co-registration are shown in Figure 3A.

After co-registration, we checked whether foveal sites have organized topography or not, and in a continuous manner with peripheral representation. We identified sites having 0.5 deg preferred visual eccentricity in their visual responses, and we then interpolated between these sites to draw a 0.5-deg iso-eccentricity line. We repeated this procedure for 1, 2, 5, 10, 20, and 40 deg eccentricities (Figure 4A). We similarly checked iso-direction lines (Figure 4B).

Finally, to obtain a mathematical fit [33], we repeated a procedure similar to that in [33]. Critically, the key element here was that we had measurements from *both* foveal and peripheral sites, unlike in [33, 35]. We first rotated the co-registered sites to make the interpolated horizontal meridian (i.e., 0 deg direction line) lie along a horizontal line (e.g., Figures 4A–4D with anatomically-accurate orientation of the horizontal meridian representation versus Figure 5A with a rotated map to align the horizontal meridian along a horizontal plotting line). We then ran Equations 1 and 2 (main text). We obtained new model parameters for the equations by minimizing the least-mean-square error from the equations to our data similarly to the original paper method. Critically, we used all of our measurements for the data fit and not just the iso-eccentricity and iso-direction. We further verified the result by plotting the new parameters on top of our data to visualize the origin of the SC, and we confirmed that the origin was not in the non-SC regions from our dense mappings. The result is shown in Figure 4C. We also confirmed that our results provide a much better fit than the original model in [33] (Figure 4D).

To estimate the size of the active population of neurons in SC tissue for a given visual stimulus location, transformation of RF shapes from visual coordinates into SC tissue coordinates is needed [25, 33, 36, 85]. Once this transformation is done, it is trivial to estimate the size of the active population for a given stimulus location: this is achieved by simply checking which neurons in the SC map would be activated by the stimulus (and to what extent according to the stimulus location relative to the RF hotspot location) based on the relative positioning between stimulus location and RF coordinates in neural tissue space [25, 33, 36, 85]. We thus converted visual RF's into SC tissue coordinates (Figure 5A). To do this, we simply plotted firing rate maps as a function of position in the SC tissue space as opposed to visual location. In other words, for every visual location at which we measured RF responses, we converted its eccentricity and direction pair (R, θ) from Equations 1 and 2 into neural tissue coordinates X and Y.

Foveal tissue magnification factor

In Figure 4E, we computed linear foveal magnification factor (mm of neural tissue in the SC map per deg of visual angle in visual space) along the horizontal meridian. We did this for the original universally accepted model of SC topography [33] as well as for our new model. We densely sampled the horizontal meridian representation in both models using 0.1 deg visual eccentricity resolution, and we plotted the difference of tissue distance from one sample to the next (appropriately dividing by the step in eccentricity to obtain a correct mm/deg measure).

In Figure 4F, we wanted to compare the linear foveal magnification factor in the SC to that in the primary visual cortex (V1). However, a direct quantitative comparison of V1 foveal magnification factor to Figure 4E would have been inappropriate and unfair because the SC is approximately an order of magnitude smaller in size than V1. Therefore, we first scaled the SC size upward in order to match the size of V1, and we then compared quantitative measures. We scaled the SC upward based on quantitative measures of V1 size. Specifically, we multiplied SC distance along the horizontal meridian by a scale factor that was based on the ratio of linear distances from 2.5 deg eccentricity to 40 deg eccentricity in both the SC and V1. In the SC, the distance (between 2.5 deg and 40 deg eccentricity lines) from our measurements was 2.8463 mm. In V1, we estimated this distance to be 25.2014 mm based on [10].

Therefore, we scaled the SC's horizontal meridian representation by a factor of 8.8541 (equal to 25.2014/2.8463) before comparing SC foveal tissue magnification to that in V1. The comparison was then done by plotting our scaled estimate of SC foveal tissue magnification (if the SC was of approximately the same physical size as V1) to V1 data reported in [11] from multiple studies (Figure 4F).

Constructing 3-dimensional SC surface topography

We used dense mappings in monkeys R and F and histological sections to develop a detailed 3-dimensional characterization of macaque SC surface topography. To register the physiological recordings to a common MRI space, we needed an intermediate step to align the anatomical locations of the recordings. In one penetration, we therefore made an electrolytic lesion close to the SC (monkey R; Figure 3A). We took all histological sections containing the SC, and we manually traced the SC border (Figure 3B). We next interpolated the outline of the SC in 3-dimensions using Free-D [61] (Figure 3B), and we used rigid body transformation to register the reconstructed 3-dimensional SC to a published normalized MRI common space for postmortem macaque monkeys [32] (Figure 3C). We used the cerebral aqueduct as our landmark and for registration with the standard MRI image. After the registration, we used the electrolytic lesion mark from monkey R to register the physiological recordings to the MRI. We also plotted the SC and non-SC regions (as identified physiologically) to confirm that our registration procedure matched with the known anatomical landmarks on the MRI image (Figure 3D; Video S1). Finally, we rendered the MRI data with ITK-SNAP [62] and plotted our new parameters on the rendered image (Figure 3E; Video S2). Data S1 contains 3-dimensional coordinates of right SC surface iso-eccentricity and iso-direction lines in our new 3-dimensional model of SC topography.

DATA AND SOFTWARE AVAILABILITY

Data S1 (separate file)

A Microsoft Excel file (related to Figure 3 and Video S2) containing tables of x, y, and z coordinates for the right SC's anatomical coordinates along with individual iso-eccentricity and iso-direction lines. The file contains a table for iso-eccentricity lines and a table for iso-direction lines. The file also contains additional tables with coordinates for the 3-dimensional anatomical SC surface (for generating Video S2), as a resource for future uses of our SC surface topography. All measurements are in millimeters (mm) relative to the anterior commissure, as explained in the file [S15].

Current Biology, Volume *29*

Supplemental Information

The Foveal Visual Representation of the Primate Superior Colliculus

Chih-Yang Chen, Klaus-Peter Hoffmann, Claudia Distler, and Ziad M. Hafed

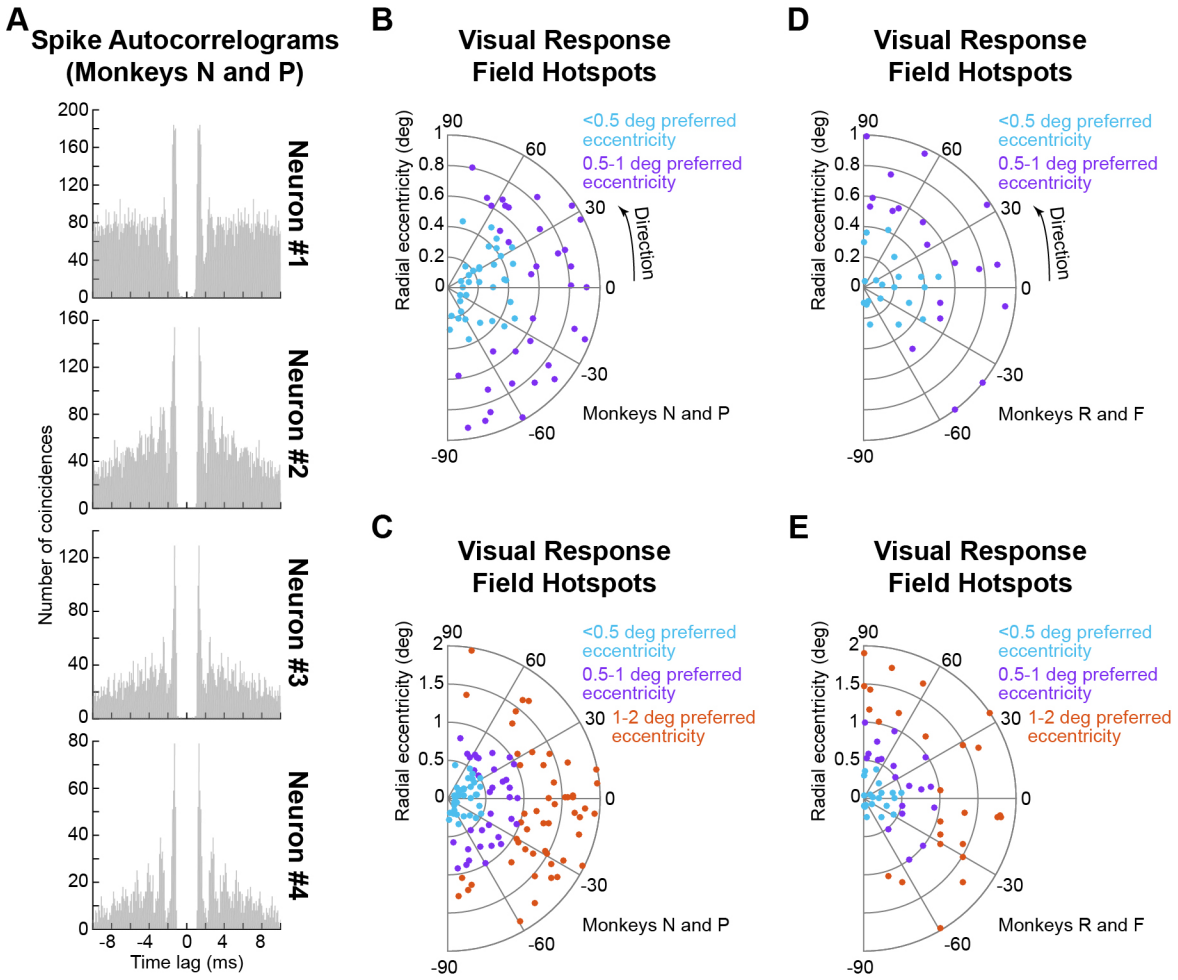

Figure S1. Online spike isolation quality for the awake monkey experiments, and sampled foveal locations represented by SC neurons in all four monkeys. Related to Figures 1, 2. (A) Spike autocorrelograms from the RF mapping tasks of Figure 1 for the four example neurons in that figure. The autocorrelograms confirm no action potentials occurring within spiking refractory periods, suggesting that the neurons (isolated online during the sessions) were well-isolated. Similar isolation quality was present across our population of awake monkey recording data. **(B)** Preferred RF hotspot locations identified in awake monkeys N and P. The neurons are color-coded according to their preferred hotspot eccentricity. We sampled a substantial number of neurons representing a region of visual space within the rod-sparse foveola area of the retinal image (<0.5 deg preferred eccentricity). **(C)** The same data as in **A** along with additional neurons (1-2 deg preferred eccentricity), demonstrating approximately uniform sampling of all possible eccentricities <2 deg. More eccentric neurons (>2 deg) are not shown, but they were included in all of our analyses for critical comparisons to foveal SC representations. Note that we recorded in both right and left SC's in each of monkeys N and P, but we rotated all neurons into one visual hemifield for figure simplicity. All neurons had visual RF hotspots that were located in the contralateral visual hemifield to the recorded SC. **(D, E)** Preferred RF hotspot locations identified in anesthetized monkeys R and F. Same formatting as in **B**, **C**. For monkeys R and F, we recorded from right SC (representing the left visual hemifield) in monkey R and left SC (representing the right visual hemifield) in monkey F, but we again rotated the data in this figure for presentation purposes.

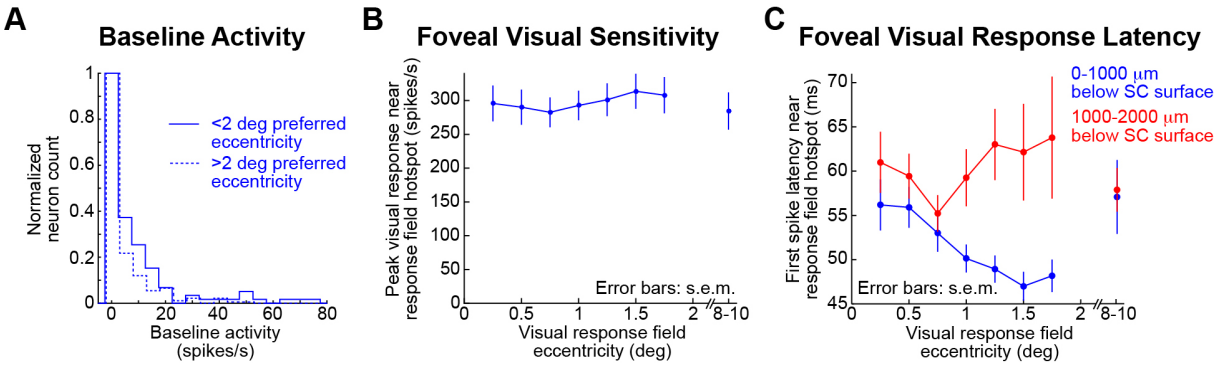

Figure S2. Visual properties of foveal SC neurons. Related to Figures 1, 2. (A) Most neurons in the awake animals, whether foveal (solid line) or eccentric (dashed line), had little baseline activity. For each neuron, we measured average firing rate within a 200-ms baseline interval in monkeys N and P (Methods: *Neuron classification*). Note that our neurons were generally shallower (e.g. Figure S4D) than deep SC neurons in earlier reports that can show tonic activity, also rostrally within this structure (e.g. [S1, S2]). **(B)** For all neurons with preferred eccentricity <2 deg (Figure S1B, C, awake monkeys N and P), we plotted peak visual response near the preferred RF hotspot location (Methods: *Visual response sensitivity and latency*) as a function of preferred eccentricity. For comparison, we also plotted visual response sensitivity for neurons preferring 8-10 deg eccentricities (again with stimuli appearing at the respective RF hotspots). SC foveal visual sensitivity was as strong as that at 8-10 deg (Ranksum test, p= 0.63753). Also, within the central 2 deg, there was no dependence of visual sensitivity on neuronal preferred eccentricity (1-way ANOVA, F=0.1924, p=0.9014). **(C)** We measured the latency to first stimulus-evoked action potential (spike) for the same locations and neurons as in **B**. In this case, we separated the neurons as being either superficial (<1000 μm below SC surface) or deeper (1000-2000 μm below SC surface) because they showed different results. Superficial neurons (blue), which are retina-recipient [S3-S5], had longer first-spike visual response latencies within the foveola region and decreased their response latency with increasing eccentricity in the rest of the central 2 deg (1-way ANOVA, F=3.4096, p=0.023). This might reflect an impact of rod-sparse foveolar cone input to neurons (whether directly or through cortex) representing <0.5 deg eccentricities. Deeper neurons (red), not receiving direct retinal input, did not show a dependence of first-spike latency on eccentricity in the central 2 deg (1-way ANOVA, F=0.7479, p=0.5288). Note also that superficial neurons responded earlier than deeper neurons in general (Ranksum test, p=0.0040, all eccentricities <2 deg; $p=6.375 \times 10^{-6}$, all eccentricities), consistent with peripheral results [S6]. Error bars denote s.e.m.

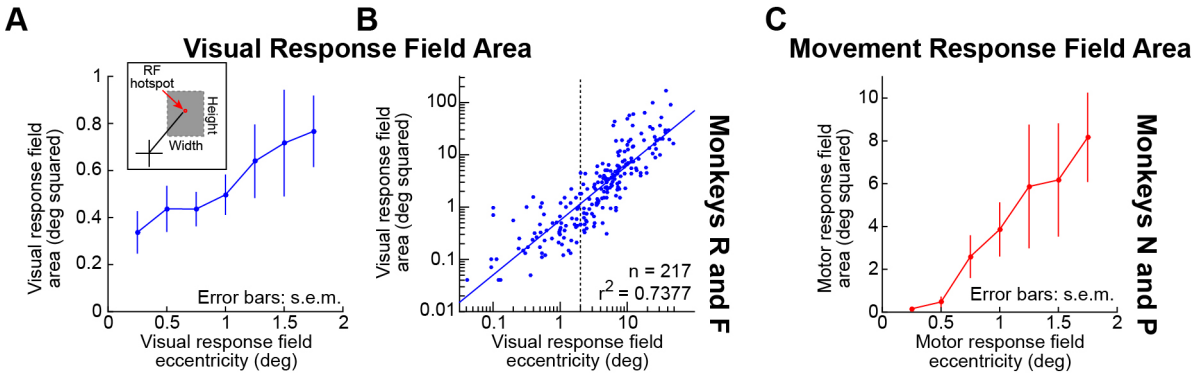

Figure S3. Non-uniform sampling within the SC foveal visual representation even in anesthetized monkeys, and also in the movement response fields of awake monkeys. Related to Figure 2. (A) For monkeys R and F, we performed similar analyses on visual RF area to those presented in Figure 2A (left) for the awake monkeys. The inset shows how we assessed RF area in these anesthetized cases (Methods: *Visual and motor RF hotspot and area calculations*). Error bars denote s.e.m. (p=0.05, 1-way ANOVA as a function of eccentricity, F=2.75, n=66). **(B)** Data from the central 2 deg are now shown along with the rest of the neurons that we sampled. Each dot represents a single penetration (as in Figure 2A, right), and we now plot data on a logarithmic scale because of the large range of eccentricities and areas that we measured. The blue line shows a linear regression fit of all data points (on the logarithmically transformed scales). Like with the awake monkeys (Figure 2A), the SC foveal visual representation formed a continuum, in terms of spatial sampling resolution, with the peripheral representation, showing a supra-linear growth in RF area as a function of increasing eccentricity. The dashed vertical line delineates the 2 deg eccentricity line. Foveal neurons (<2 deg preferred eccentricity) clearly showed non-uniform sampling resolution, like in the peripheral representation, and also like in the awake animals (Figure 2A). Note that we did not quantitatively compare RF areas between awake and anesthetized animals due to several experimental constraints (Methods: *Visual and motor RF hotspot and area calculations*). **(C)** Non-uniform spatial sampling within the SC representation of foveal space even for movement-related RF's. For the awake monkeys N and P, we measured microsaccade- and saccade-related responses (Methods: *Neuron classification*), and we performed the same RF area analyses on these responses. Within the foveal representation, we observed similar non-uniform sampling resolution, in terms of RF area, to that we observed for visual RF's (e.g. compare to Figure 2A and **A**, **B**) ($p=1.260\times10^{-3}$, 1-way ANOVA as a function of eccentricity, F=6.05, n=58). Note that microsaccade-related movement RF's in the fovea (<1 deg) were smaller than visual RF's in the same animals (Ranksum test, $p=2.180\times10^{-5}$) [S7, S8]. Error bars denote s.e.m.

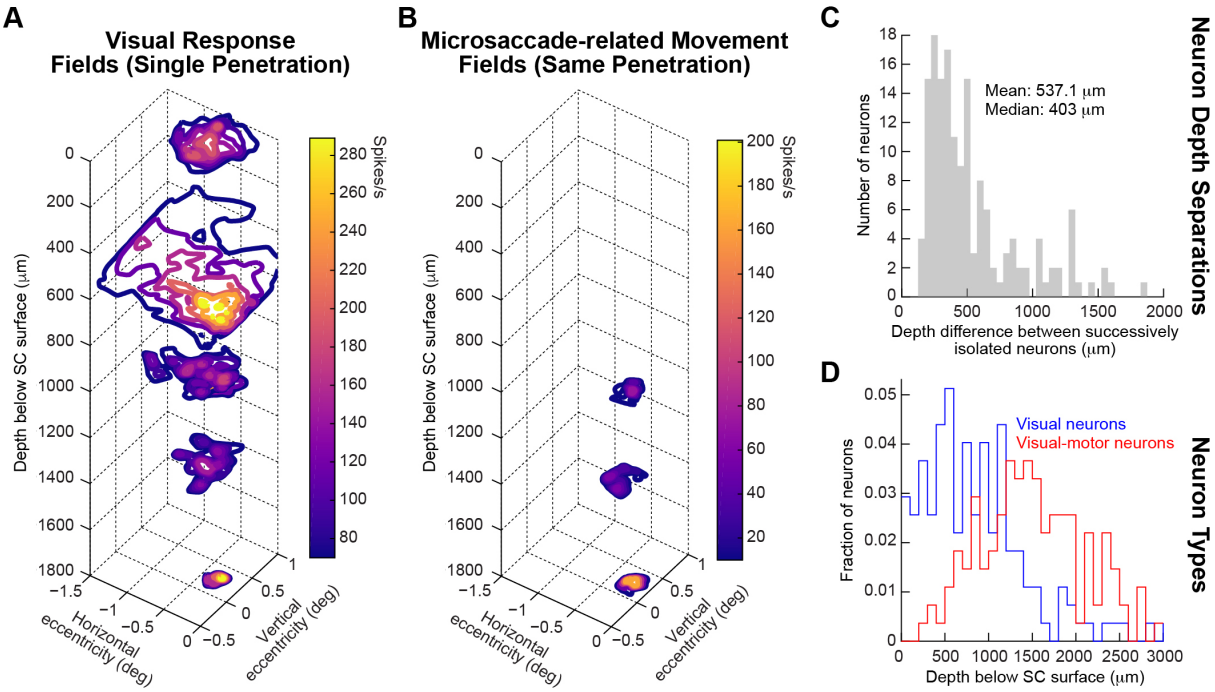

Figure S4. Consistent vertical organization of visual and visual-motor neurons within the SC's foveal representation. Related to Figures 1, 2. (A) Example visual RF maps from 5 different neurons isolated within the same recording session in an awake monkey, as the recording electrode was advanced deeper and deeper into the SC (Methods: *Behavioral tasks for awake experiments*). Each plane along the z-axis plots a pseudocolor surface describing peak visual response after stimulus onset (color-coded) as a function of horizontal and vertical target eccentricity (x- and y-axes). The z-axis plane at which each surface is drawn indicates the depth at which the neuron was encountered relative to SC surface. As can be seen, neurons within a single "depth column" of the SC had similar preferred eccentricities, consistent with peripheral SC representations. **(B)** The three deepest neurons from **A** also had microsaccade-related movement RF's (Methods: *Neuron classification*) [S7, S8]. Thus, the most superficial two neurons were purely visual neurons (no movement-related discharge), whereas the deeper three neurons were visual-motor neurons. This ordering of visual and visual-motor neurons is consistent with peripheral SC depth-related organization [S9]. **(C)** For the sessions in the awake animals in which we recorded multiple neurons, we plotted the distance (along the electrode depth dimension) between two successively recorded neurons. This tended to be ~500 μm on average. Note that since the SC is a humped structure, these depth separation estimates may not always be orthogonal to the anatomical SC layers, since our recording chamber was flat. However, combined with Figure 3 and Data S1, they can nonetheless give a sense of how one might expect to encounter neurons while recording deeper and deeper from the (foveal) SC. **(D)** In the awake animals, we observed an expected relationship (as in **A**) between neuron depth from SC surface and whether it exhibited movement-related discharge in addition to visual sensitivity. The shown distribution combines foveal and eccentric neurons.

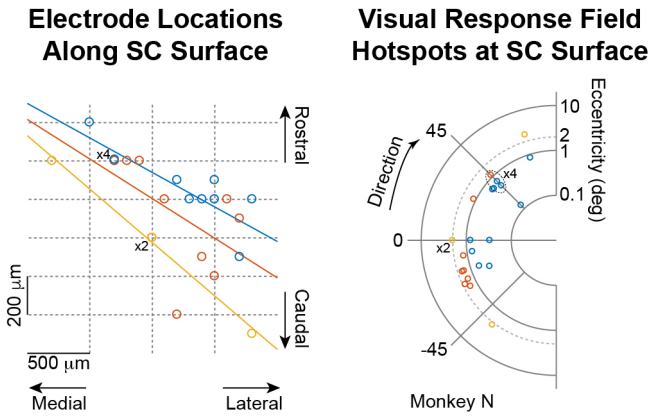

Figure S5. Orderly topographic organization within SC foveal visual representation even in awake monkeys. Related to Figure 4. We took a contiguous series of 24 back-to-back awake-monkey recording experiments, in which we systematically sampled within the rostral region of a single SC (the right SC) of a single monkey (monkey N). In the left panel, we plotted penetration locations within the recording chamber (the chamber was placed on the midline and tilted 35 deg posterior of vertical in this animal; Methods: *Animal preparation for awake experiments*), and we color-coded the penetration locations according to the preferred visual eccentricities encountered in the most superficial SC laminae. Two sites were visited multiple times, as indicated (the site visited 4 times slightly displaces the different colored circle for visibility). The preferred eccentricities are plotted in visual coordinates in the right panel (using a logarithmic eccentricity scale); the preferred eccentricity estimates for the sites visited multiple times are highlighted (demonstrating repeatability of the experiments). The colored lines in the left panel are linear regression lines for each color coding of penetration location, demonstrating orderly clustering of iso-eccentricity sites, and with an anatomical orientation (relative to the rostral-caudal axis) similar to that seen in the anesthetized animals (Figure 4A-D). We also observed that medial sites represented upward directions from horizontal and lateral sites represented downward directions. Note that a direct comparison of the left panel in this figure to Figure 4 is not appropriate because of the different penetration angles in the two cases.

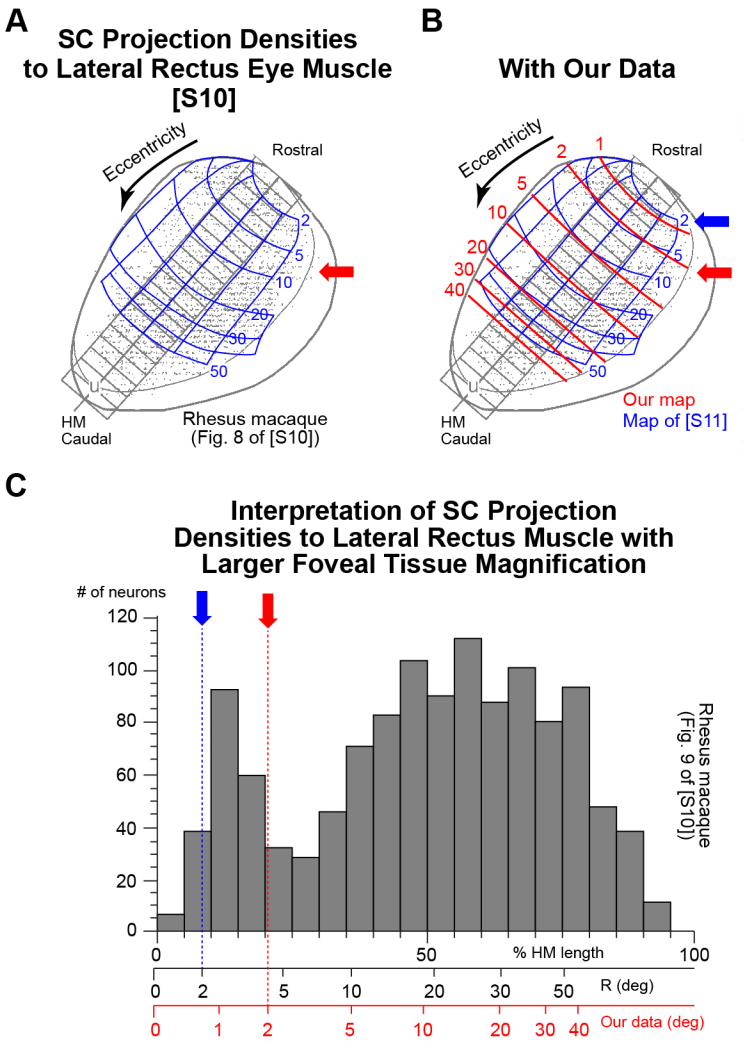

Figure S6. Recasting interpretations of SC efferent projections to the oculomotor periphery. Related to Figure 4. (A) Besides comparisons to primary visual cortex (V1), a potential source of afferent input to the SC (Figure 4F), we also explored the implications of larger foveal magnification on interpreting efferent SC projections. The figure, adapted with permission from [S10], shows retrograde labeling from the lateral rectus eye muscle (driving horizontal eye movements) to the SC with Rabies virus (gray dots). Blue is Grantyn et al.'s [S10] estimate of topography, based on [S11], and the diagonal grid is their binning of tissue for the measurements in **C**. HM means horizontal meridian. The red arrow shows the 2-deg eccentricity line according to our more complete measurements of SC topography (Figures 3-5, S5), if our map is aligned at the origin with the Robinson map alignment (as in Figure 4D); this demonstrates how the interpretation of raw cell densities (gray dots) can be grossly misestimated. **(B)** This is better illustrated when our map is superimposed in red, again when the origin was aligned to the same origin of the blue map. **(C)** Histograms of the cell densities from **A**, **B** along the horizontal meridian. With the original map placement (black horizontal axis of eccentricity), it may appear that the central 5 deg of SC representation are a distinct zone because of the bimodal distribution dip near 5 deg in the black horizontal axis. However, with our more complete mapping of SC topography, the distinct zone transition in cell densities may delineate a much smaller eccentricity (red arrow).

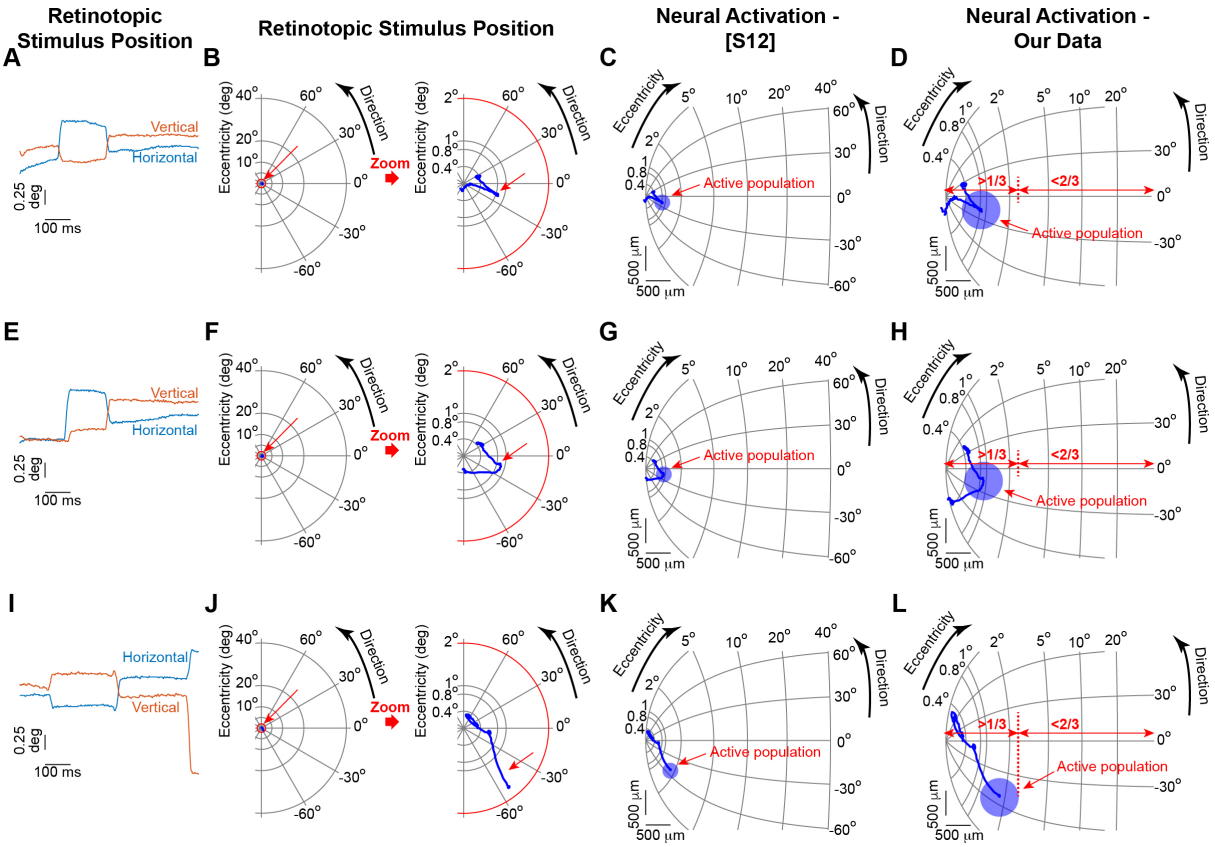

Figure S7. SC activation when tiny fixational eye movements shift retinal images. Related to Figures 4-6. The combination of foveal magnification (Figures 4, 5) and eye movements (Figure 6) means that even small foveal stimuli can cause significant activation waves. The figure shows how the retinal image of a small foveal spot gets moved around by fixational eye movements and what this means in neural tissue coordinates. **(A)** Retinotopic stimulus position in one example trial of a small stationary spot (e.g. Figure 6A). **(B)** The left panel shows the motion trajectory (blue) from **A** in retinotopic visual field coordinates. The spot was initially place at 0.4 deg before being shifted around by fixational eye movements, and the small red circle delineates 2 deg. Relative to the entire visual field (left panel), the motion trajectory (blue) was barely visible. The right panel magnifies the central 2 deg to highlight the small motion. **(C)** The motion of the spot on SC tissue as per the classic model of [S12]. The blue circle demonstrates an estimate of the active population (e.g. Figure 5) at a specific time during the trial. **(D)** A more accurate depiction of stimulus trajectory from the same trial based on our dense mapping of SC foveal topography (Figures 4, 5). A simple foveal stimulus can activate up to ~1 mm of SC tissue due to small fixational eye movements. **(E-H)** Same for another example trial. **(I-L)** Same for another example trial. Note how the edge of the active population (red dashed vertical line) can reach a distance greater than 1/4-1/3 of the entire SC rostral-caudal extent. Also note that in real neural dynamics, there can be even longer range interactions than simply stimulus position [S13, S14]. SC maps were rotated as in Figure 5 such that the eccentricity dimension was on the horizontal dimension.

Supplemental References

S1. Krauzlis, R.J., Basso, M.A., and Wurtz, R.H. (1997). Shared motor error for multiple eye movements. Science *276*, 1693-1695.

S2. Krauzlis, R.J., Basso, M.A., and Wurtz, R.H. (2000). Discharge properties of neurons in the rostral superior colliculus of the monkey during smooth-pursuit eye movements. J Neurophysiol *84*, 876-891.

S3. Schiller, P.H., Malpeli, J.G., and Schein, S.J. (1979). Composition of geniculostriate input ot superior colliculus of the rhesus monkey. J Neurophysiol *42*, 1124-1133.

S4. Pollack, J.G., and Hickey, T.L. (1979). The distribution of retino-collicular axon terminals in rhesus monkey. J Comp Neurol *185*, 587-602.

S5. Wilson, M.E., and Toyne, M.J. (1970). Retino-tectal and cortico-tectal projections in Macaca mulatta. Brain Res *24*, 395-406.

S6. Chen, C.Y., Sonnenberg, L., Weller, S., Witschel, T., and Hafed, Z.M. (2018). Spatial frequency sensitivity in macaque midbrain. Nat Commun *9*, 2852.

S7. Hafed, Z.M., Goffart, L., and Krauzlis, R.J. (2009). A neural mechanism for microsaccade generation in the primate superior colliculus. Science *323*, 940-943.

S8. Hafed, Z.M., and Krauzlis, R.J. (2012). Similarity of superior colliculus involvement in microsaccade and saccade generation. J Neurophysiol *107*, 1904-1916.

S9. Wurtz, R.H., and Goldberg, M.E. (1971). Superior colliculus cell responses related to eye movements in awake monkeys. Science *171*, 82-84.

S10. Grantyn, A., Brandi, A.M., Dubayle, D., Graf, W., Ugolini, G., Hadjidimitrakis, K., and Moschovakis, A. (2002). Density gradients of trans-synaptically labeled collicular neurons after injections of rabies virus in the lateral rectus muscle of the rhesus monkey. J Comp Neurol *451*, 346-361.

S11. Robinson, D.A. (1972). Eye movements evoked by collicular stimulation in the alert monkey. Vision Res *12*, 1795-1808.

S12. Ottes, F.P., Van Gisbergen, J.A., and Eggermont, J.J. (1986). Visuomotor fields of the superior colliculus: a quantitative model. Vision Res *26*, 857-873.

S13. Chen, C.Y., Ignashchenkova, A., Thier, P., and Hafed, Z.M. (2015). Neuronal Response Gain Enhancement prior to Microsaccades. Curr Biol *25*, 2065-2074.

S14. Chen, C.Y., and Hafed, Z.M. (2017). A Neural Locus for Spatial-Frequency Specific Saccadic Suppression in Visual-Motor Neurons of the Primate Superior Colliculus. J Neurophysiol, jn 00911 02016.

S15. Calabrese, E., Badea, A., Coe, C.L., Lubach, G.R., Shi, Y., Styner, M.A., and Johnson, G.A. (2015). A diffusion tensor MRI atlas of the postmortem rhesus macaque brain. Neuroimage *117*, 408-416.